ETH zürich

Transient Electromagnetic Simulations of Linear Induction Motors (LIMs)

SEMESTER THESIS

Presented by: Matthias Strässle

Supervised by: Prof. Dr. Jasmin Smajic

Prof. Dr. Juerg Leuthold

May 2020

swissloop

Institute of Electromagnetic Fields (IEF)

ETH zürich

Semester Project

Transient Electromagnetic Simulations of Asynchronous Linear Motors (ALIMs)

Student
Matthias Strässle (D-ITET)

Volume
12 ECTS

Type of Work
Theory & Simulation

Requirements
Experience in physical modeling and simulation are advantageous.

State-of-the-art
Linear induction motors (LIM) attract presently a considerable attention in the area of future vacuum transportation technologies and systems. There are several reasons for this tendency: (a) LIMs are simple and inexpensive, (b) use the supporting rail as a moving part of the motor, and (c) leave the induced losses in the mover (rail) outside of the motor reducing consequently its temperature.

LIMs have a nonlinear thrust-speed characteristics, require very careful and demanding electromagnetic simulations during their development, and need very advanced vector control for obtaining a high acceleration rate.
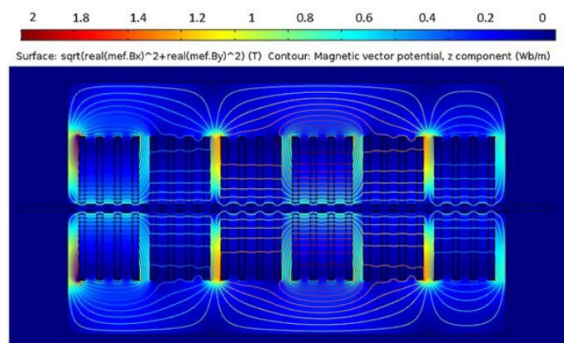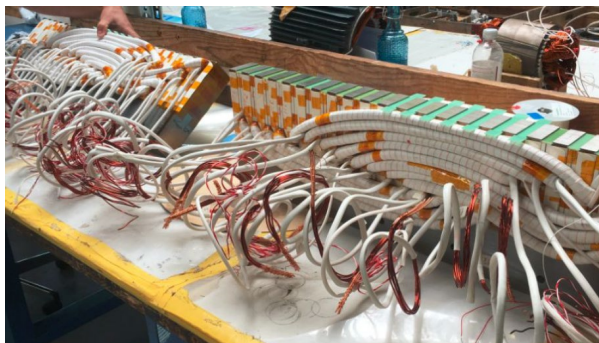
Figure 1. Double sided linear induction motor (LIM1, developed within a collaboration between IEF and Swissloop for the Hyperloop competition of Elon Musk in LA) in its final stage production (left) is presented. The magnetic flux density distribution in the LIM1 is shown (right). More details can be found in the online article.

Thesis Description

The thesis has the following main goals
- Transient electromagnetic simulation of the downsized LIM (baby-LIM) with the original winding topology in order to obtain its nonlinear thrust-speed characteristic.
- Comparison of the numerical simulation results against the available measurements performed on the baby-LIM.
- Time domain FEM simulations of the motor transients arising from pole-pair switching during vehicle motion at a given initial speed. This simulation scenario is relevant for the foreseen new control of the motor.

ETH Zurich
Dr. Jasmin Smajic, ETZ K 90
Prof. Dr. Juerg Leuthold, ETZ K 81
Gloriastrasse 35
8092 Zurich

Phone: +41 44 633 89 88
Email: smajicj@ethz.ch

www.ief.ee.ethz.ch ➔ Education ➔
Semester and Master Projects

Institute of Electromagnetic Fields (IEF)

ETH

Eidgenössische Technische Hochschule Zürich
Swiss Federal Institute of Technology Zurich

Declaration of originality

The signed declaration of originality is a component of every semester paper, Bachelor's thesis, Master's thesis and any other degree paper undertaken during the course of studies, including the respective electronic versions.

Lecturers may also require a declaration of originality for other written papers compiled for their courses.

I hereby confirm that I am the sole author of the written work here enclosed and that I have compiled it in my own words. Parts excepted are corrections of form and content by the supervisor.

Title of work (in block letters):

Transient Electromagnetic Simulations of Linear Induction Motors (LIMs)

Authored by (in block letters):
For papers written by groups the names of all authors are required.

Name(s):   **First name(s):**
Strässle   Matthias

With my signature I confirm that
- − I have committed none of the forms of plagiarism described in the 'Citation etiquette' information sheet.
- − I have documented all methods, data and processes truthfully.
- − I have not manipulated any data.
- − I have mentioned all persons who were significant facilitators of the work.

I am aware that the work may be screened electronically for plagiarism.

Place, date   **Signature(s):**
Winterthur, 25.05.2020   Matthias Strässle

For papers written by groups the names of all authors are required. Their signatures collectively guarantee the entire content of the written paper.

Abstract

Since 2016 Swissloop has designed, built, and tested prototype pods for Hyperloop systems. In 2019/2020 a novel Linear Induction Motor (LIM) was designed to be built into the newest prototype. Sadly the Hyperloop Pod Competition 2020 was canceled and this led to the production of a downsized version of this LIM. In this thesis this downsized LIM is simulated and the different simulation-types are compared and evaluated. In a second step, simulations of a pole-pitch-transition are done, what the initial LIM was designed for. This allows for lower frequencies at high speeds. Finally, the possibility of magnetic levitation with the designed LIM is investigated. The results provide valuable information for the development of the next generation LIM for Swissloop prototypes.

Due to unfortunate circumstances, the part related to testing the BabyLIM could not be addressed and alternatively the topic of levitation with a LIM has been added.

Abstract

Acknowledgments

I would like to thank the Institute of Electromagnetic Fields (IEF), along with Prof. Leuthold and Dr. Jasmin Smajic, for supporting this thesis. The valuable support and advice throughout my work was very educational.

Further, I would like to thank the entire Swissloop team. The interesting discussions were always very enlightening and helped me to achieve my goals. Thank you Nicholas Marchal and the Swissloop team 18/19 for the incredible foundation you made with the LIM19. Thank you Philip Wiese for designing the LIM20 with me, which was the foundation for this thesis. Thanks to Michael Rogenmoser for designing a capable inverter and leading our electrical team. Thank you Yvan Bosshard, to design the control systems for this complex structure. And thank you Thomas Umbach and Colin Lienhard for constantly adapting to modifications, and designing the mechanical integration for this LIM.

A special thanks to Gebrüder Meier AG who built the BabyLIM, and of course the various other Swissloop partners. Without them such a project would not be possible.

Last but not least, I would like to thank my family and friends for supporting me in every aspect.

Acknowledgments

Contents

Contents

1 Introduction

One of the biggest challenges for this generation is the reduction of greenhouse gas emissions. Transportation plays a big part in carbon emission. Close to 25 % of greenhouse gas emissions in the EU came from this sector [1]. As combustion engine cars and planes are nearly as efficient as they can possibly be, new ideas to revolutionize this sector are needed.
The idea to get from one point to another faster has always been interesting to humans. It led to the invention of the wheel in the early days and followed up with trains and cars. With increasing technologies and faster speeds one had to include drag into the equation. Nowadays, the drag produced by air is one of the limiting factors for how fast a car can drive. Even though air drag can be reduced efficiently with aerodynamics, it is not possible to reduce it to zero. The idea to reduce drag with vacuum-based transportation dates back to the 19th century. At that time technology wasn't advanced enough to construct such a system and therefore the idea was never fully realized [2].

In 2013 Elon Musk revived the concept of vacuum-based transportation with his white paper "Hyperloop Alpha" [3]. The concept thereby is to place a pod (transport capsule) in a vacuum tube and accelerate it to a velocity near the speed of sound. While a perfect vacuum is difficult to create and maintain, a low-pressure environment is proposed. To reduce drag further, the concept calls for contactless levitation, stabilization, and propulsion methods. Unfortunately, industry did not follow the call and therefore Elon Musk launched the "SpaceX Hyperloop Pod Competition" in 2015 [4]. In this gathering, student teams from all over the world design and build a pod to do research on the hyperloop concept. After competing in a series of tests, the best teams get to race their pods against each other in the 1.2 km vacuum test track in Hawthrone, California. The goal of this competition is to promote research in vacuum-based transportation technology.

1.1 Linear Induction Motor

A powerful contactless propulsion system is the LIM. With this technology it is possible to perform a translation without the usual rotary elements and the friction, that comes with it, in typical electric motors. The full theory for LIM is given in chapter 2. Nevertheless, a small introduction into the working principle of such a motor will be given here to understand the challenges that come with it.

A LIM can be imagined as a conventional rotary asynchronous machine cut to the center and bent straight. A LIM of this form with one primary (stator) and one secondary (rotor) is called Single-Sided Linear Induction Motor (SSLIM) (Fig. 1.1a). On the other side of the secondary an iron sheet is placed to better guide the fields. By adding a second primary instead of the iron backplate the Magnetomotive Force (MMF) can be doubled and with it the generated thrust. Such a design is called a Double-Sided Linear Induction Motor (DSLIM) (Fig. 1.1b). In order to move the primary or secondary, one has to be longer than the other. Therefore,
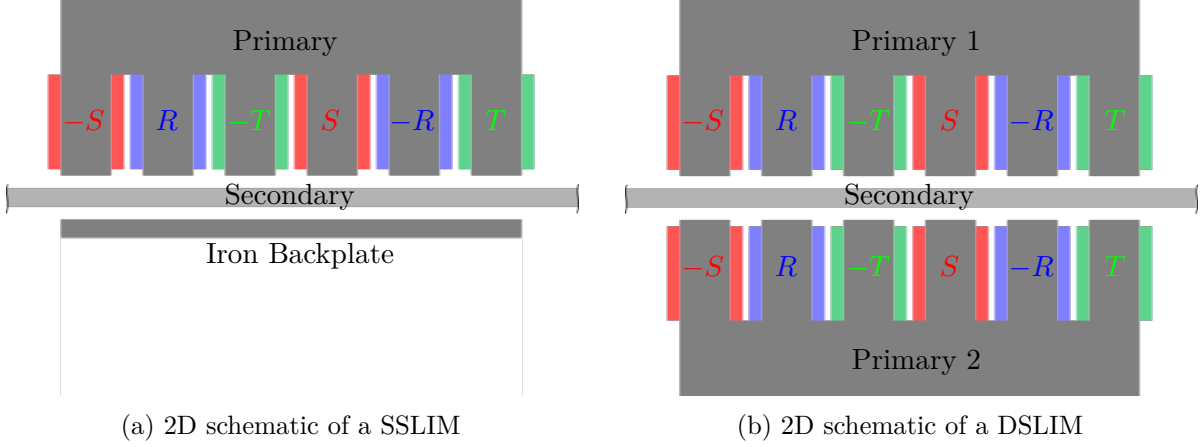
(a) 2D schematic of a SSLIM

(b) 2D schematic of a DSLIM

Figure 1.1: Two design types of a short primary LIM with the corresponding current phases when all coils are wounded in the same direction.

two basic types of LIMs can be distinguished: a short primary and a short secondary. Both design types can either be a SSLIM or a DSLIM. This thesis will focus on short primary motors even though most of the calculations can directly be transferred to a short secondary design by minor changes.

The primary side of the LIM consists of an iron core, usually made of sheets to reduce losses due to eddy currents, and multiple coils. By introducing a time varying sinusoidal three-phase current into the coils a sinusoidal time-varying moving magnetic field is produced. The number of full sinusoidal cycles and accordingly the number of north-south-poles is called pole-pairs p. With time the magnetic field is moving along the primary side with a speed of

$$v_s = 2\tau_p f_p \ , \tag{1.1}$$

where the pole-pitch τ_p is the distance between one north- and south-pole and f_p is the frequency of the primary three-phase current [5]. v_s is called the synchronous speed. Thrust is only generated if the speed of the LIM is smaller than this synchronous speed. The typical thrust curve of an asynchronous machine in respect to speed and slip s is given in Fig. 1.2. The slip indicates how much the speed differs from the synchronous speed and is defined as

$$s = \frac{v_s - v}{v_s} \ , \tag{1.2}$$

with the synchronous speed v_s and the mechanical speed v at which the motor is currently moving [6].

1.2 Swissloop

Swissloop [7] is a student-run organization at ETH founded in 2016 that specialized in the design of vacuum transportation pods and have successfully participated in the SpaceX Hyperloop Pod Competition since 2017. In 2019, Swissloop was amongst the first to implement a LIM into their pod named *Claude Nicollier*. With this motor and a custom-designed inverter they achieved
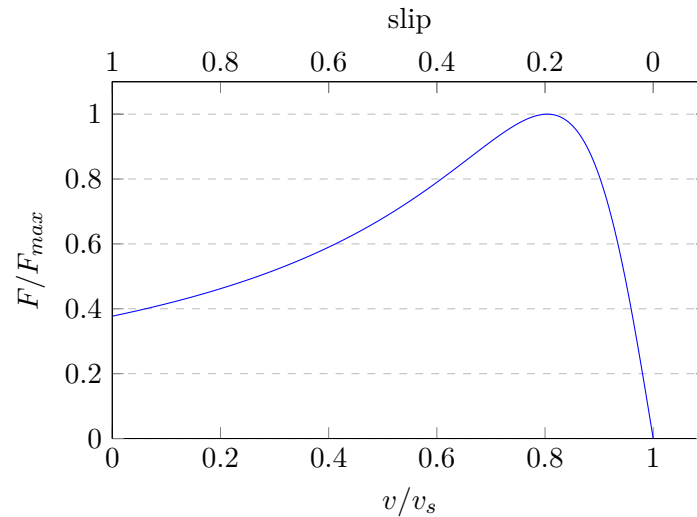
Figure 1.2: Thrust of an asynchronous machine for a constant frequency [6].

over $250\,\mathrm{km\,h^{-1}}$ and got 2nd in the competition. Additionally, they received an innovation award for the implementation of those technologies.

1.2.1 Pod Propulsion 2019

For its propulsion design of 2019 Swissloop used a motor with two primary sides placed on the pod, while the secondary is a fixed aluminum I-beam in the vacuum test track. The motor is therefore a short primary DSLIM shown in Fig. 1.3 and will further on be called LIM19.

LIM19 consists of 6 pole-pairs. The two primary sides are handled separately by an individual three-phase inverter and the phases are connected in a star-topology. This topology is shown in Fig. 1.4. For simplicity the two primary sides of the LIM are drawn as three inductors connected
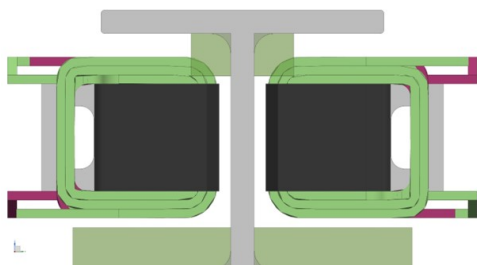
(a) Schematic with an I-beam as secondary in the middle
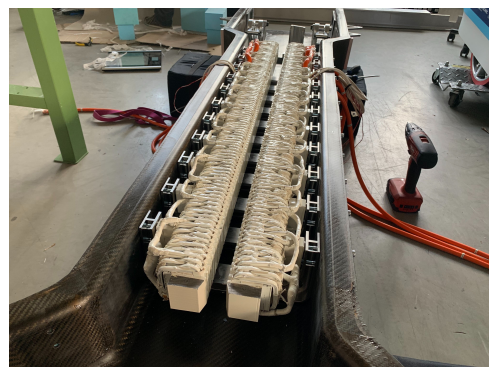
(b) LIM19 assembled in the pod

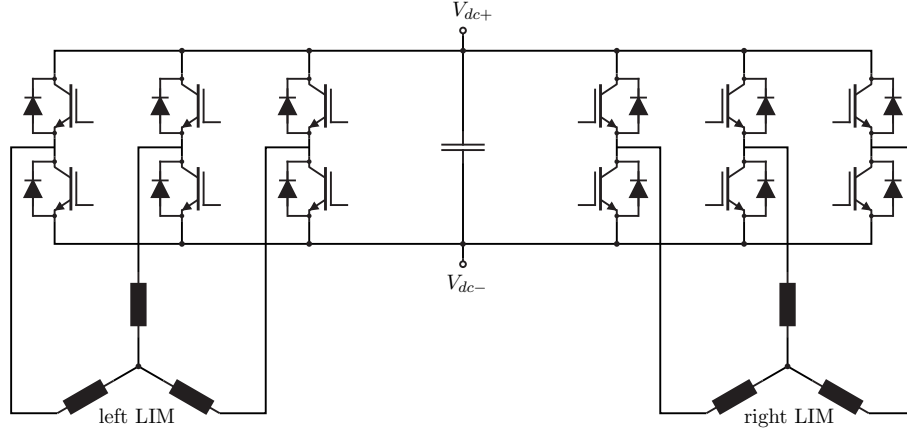Figure 1.3: LIM of the Swissloop propulsion system 2019.

Figure 1.4: Inverter topology 2019

in star. To ensure that both sides are driven by the same current, a single microcontroller was used to send the same Pulse Width Modulation (PWM) signals to both inverters [8].

Several points for improvement for the LIM19 were identified following the final run at the 2019 Hyperloop competition [4]. Most importantly, very high voltages were required to drive the motor at high speeds [8]. This is due to the high frequencies needed at higher speeds. LIM19 has a pole-pitch of $\tau_p = 91\,\text{mm}$. With equation 1.1 a frequency of $f_p > 381\,\text{Hz}$ is required to reach a speed of $250\,\text{km}\,\text{h}^{-1}$. To drive a sinousoidal current of $I_{peak} = 400\,\text{A}$ with this frequency through an inductor with $1\,\text{mH}$ a peak voltage of $v_{peak} = j \cdot \omega \cdot L \cdot i_{peak} = 1920\,\text{V}$ is required. Since a LIM has an inductive behaviour three possible interventions arise:

1. reduce the inductance.

2. reduce the needed frequency for higher speeds.

3. reduce the current needed.

4. use higher voltages (more batteries).

Further on, by rising the motor frequency the switching frequency rises as well and is always kept at a rate 10 times higher than the motor frequency. In the IGBT modules used for the inverter the current switching is the biggest source of loss. This has to be accounted for, which, in 2019, was done by installing a big heat sink.

1.2.2 Pod Propulsion 2020

In the season 2019/2020, Swissloop aimed to continue the successful idea of a LIM taking into account the lessons learned in the previous year. The goal thereby is to provide a foundation for research on new propulsion concepts and therefore building a new LIM and a new inverter. With this in mind the Swissloop team designed a novel type LIM called Software-Defined Linear Induction Motor (SDLIM) (or LIM20). The idea of this concept is to develop a motor of the
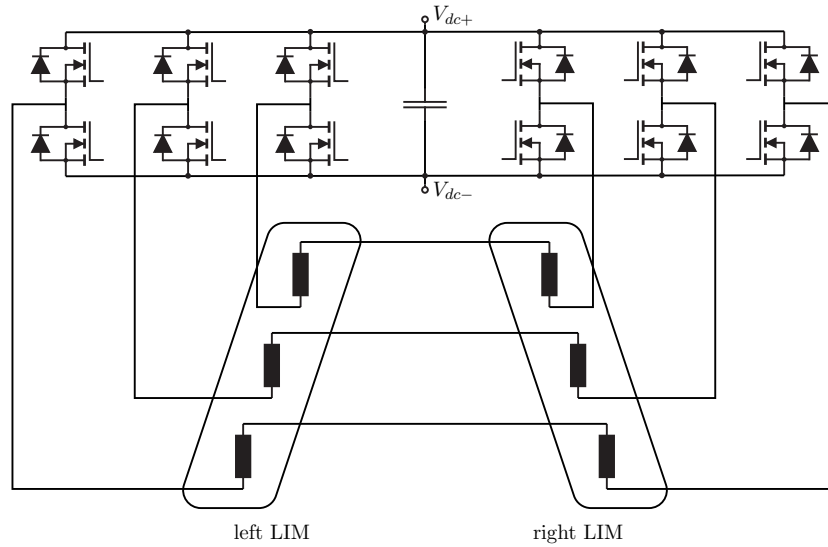
Figure 1.5: Electrical layout for one pole of the LIM20

same behavior as the former at low frequencies, but with a change in at higher frequencies. As soon as maximum voltage is reached the pole-pitch of a SDLIM can be changed in such a way, that lower frequencies can be used to further accelerate the pod. This is called "Dynamic Pole-Pitch-Transition" and will further be investigated in the last part of this thesis.

Dynamic Pole-Pitch Transition is only possible if more than three phases are used. Therefore, a new scalable high-power multi-phase variable frequency inverter was designed [8] and with it the SDLIM. In contrast to the LIM19, where the windings were around the yoke, this LIM has its windings around the teeth (Fig. 1.6). This allowed more winding-turns and therefore a smaller current to be handled by the inverter. To ensure the same current on both sides of the LIM the corresponding coils from the left and right side were connected in series and then driven by one full-bridge phase-leg of the inverter (Fig. 1.5).
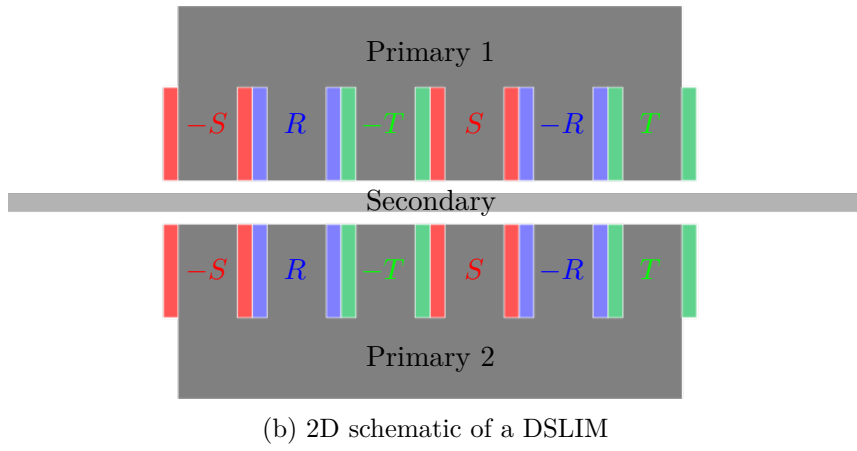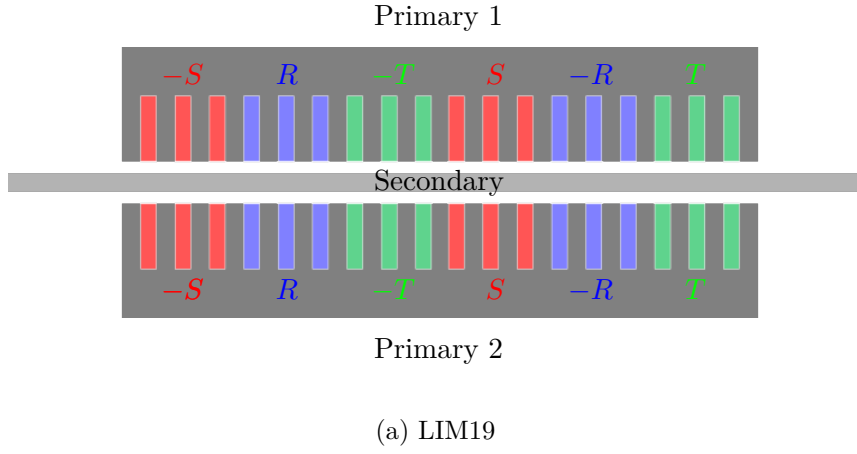
Primary 1

Secondary

Primary 2

(a) LIM19

(b) 2D schematic of a DSLIM

Figure 1.6: One pole-pair with the corresponding winding topologies of the LIM19 and LIM20.

2 Theory of Linear Induction Motors

For further understanding it is necessary to give an insight into the theory of a LIM. This chapter introduces the physical working principles of an induction machine by using Maxwell's Equations and the Lorentz Force. As discussed in chapter 1 it will be based on a short primary LIM as shown in Fig. 1.1. The theory will then be derived in a general fashion such that it can be applied to a Single- or Double-Sided-LIM. Most of this theory is abbreviated from the "Theory of Linear Induction Motor (LIM)" by Dr. Jasmin Smajic [9].

2.1 Magnetomotive Force

The MMF is the driving force for the magnetic field in a magnetic circuit. It can be compared to the voltage in an electric circuit. For a single coil the MMF (θ) is

$$\theta_{coil} = k_w N I \, , \tag{2.1}$$

where N is the number of turns, I is the current and k_w is the winding factor. $N \cdot I$ is also called "ampere-turns" (At). The winding factor k_w for linear motors is described as

$$k_w = k_p k_d \, , \tag{2.2}$$

where the pitch factor is

$$k_p = sin(\frac{\pi \tau_c}{2\tau_p}) \tag{2.3}$$

and the distribution factor is $k_d \approx 1$ [10]. The pole-pitch τ_p is the distance between two poles and the coil-pitch τ_c is the distance between the windings of the different phases.

In the case of a LIM the driving force of the magnetic field are the coils in the primary side. By looking separately at the excitation of the three phases in the LIM shown in Fig. 1.1a, each winding generates a time and place dependent MMF.

$$\theta_R(x,t) = A \sin(\omega t) \sin(\frac{\pi}{\tau_p}x) \tag{2.4}$$

$$\theta_S(x,t) = A \sin(\omega t - \frac{2\pi}{3}) \sin(\frac{\pi}{\tau_p}x - \frac{2\pi}{3}) \tag{2.5}$$

$$\theta_T(x,t) = A \sin(\omega t - \frac{4\pi}{3}) \sin(\frac{\pi}{\tau_p}x - \frac{4\pi}{3}) \tag{2.6}$$

with

$$A = \sqrt{2} \, a_1 k_w N I_{rms} \tag{2.7}$$

while N is the number of turns per winding and a_1 is the Fourier coefficient for the fundamental frequency of the real MMF. The real MMF generated by one phase is close to a rectangular shaped function. To make a full analysis of the magnetic field a Fourier transformation should

be applied and the analysis done for each frequency. An analysis with the fundamental frequency and the winding factor is accurate enough for this purpose and therefore only those will be taken into account. The MMF of phase R is illustrated in Fig. 2.1.

Equations (2.4) – (2.6) written in exponential form and added up, result in the total MMF phasor

$$\underline{\theta_{tot}}(x,t) = \frac{3}{2}A\mathrm{e}^{\mathrm{j}(-\omega t + \frac{\pi}{\tau_p}x)} \ . \tag{2.8}$$

By looking at the maximum of the MMF it can be shown that it propagates along the x-axis over time. The speed at which it travels can be calculated as

$$\exp\mathrm{j}(-\omega t + \frac{\pi}{\tau_p}x) = 1 \quad \Rightarrow \quad -\omega t + \frac{\pi}{\tau_p}x = 0 \tag{2.9}$$

and therefore

$$v_s = \frac{x}{t} = 2\tau_p f \ . \tag{2.10}$$

v_s is called the synchronous speed of the motor because, if the motor drives with this speed it would be as fast as the magnetic field. The normalized difference between the motor speed and the synchronous speed is called the slip s and can be used to describe the different operating ranges.

$$s = \frac{v_s - v}{v_s} \tag{2.11}$$

For $0 < s < 1$ the LIM is in motor-mode. A slip $s < 0$ means it has the function of a generator and for $s > 1$ a negative speed relative to the speed of the field is implied and the motor is braking.

2.2 Electromagnetic Inductance

Ampere's Law tells us that the MMF generated in an area is equal to the closed line integral of the magnetic field strength on the border of this area. Displacement currents are neglected.

$$\oint_{\partial A} \mathbf{H}\,\mathrm{d}\mathbf{l} = \iint_A \mathbf{J}\,\mathrm{d}\mathbf{A} \tag{2.12}$$

Applying this to the closed curve (C) in Fig 2.2 results in

$$H_y(x,t)\delta - H_y(x+dx,t)\delta = \theta_{tot}(x,t)\frac{dx}{\tau_p} + J_z(x,t)d_r\,dx \ . \tag{2.13}$$

Three assumptions were made to lead to this result: $\mu_{r,fe} \gg 1$, $dx \ll \tau_p$ and $J_z = const.$ over d_r. The relative permeability of iron is $\mu_r \approx 200\,000 \gg 1$. The result of which is that $H_{fe} \ll H_{air}$ and therefore only the magnetic field strength in the air gap needs to be considered. By defining $dx \ll \tau_p$, the MMF can be seen as constant over dx. $\theta_{tot}(x,t)$ contains the total amount of current distributed over one pole at a given time and place and so it must be divided by the pole-pitch to get the linear current density that is desired.

If a DSLIM is considered, the total amount of MMF generated in the primary sides is doubled and this multiplies $\theta_{tot}(x,t)$ by a factor of two. This will be further implemented as the number
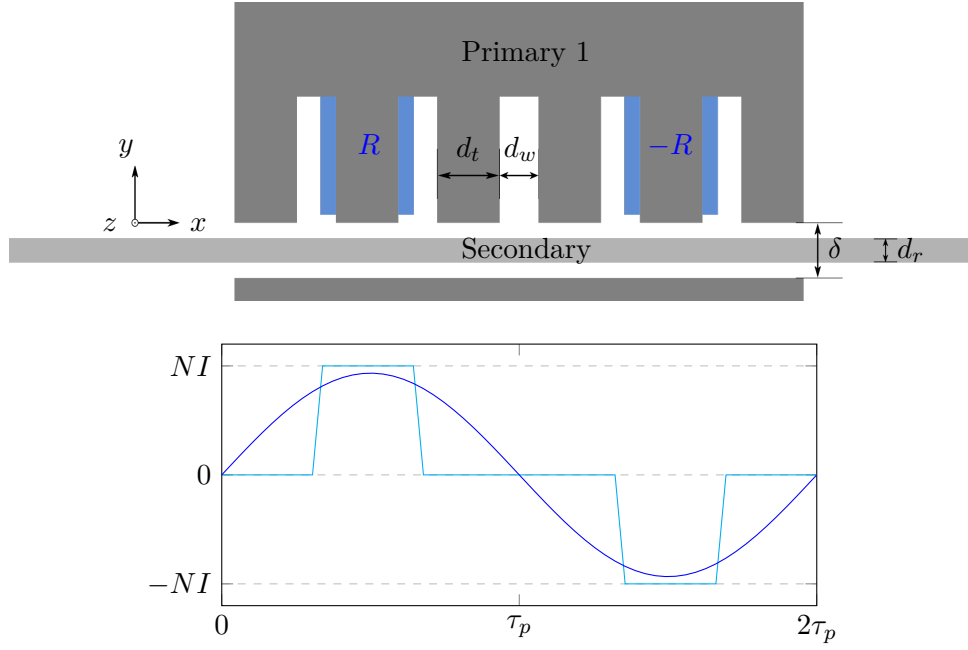
Figure 2.1: The real MMF and the first harmonic of phase R over one pole-pair at the time $t = 0.25T$.
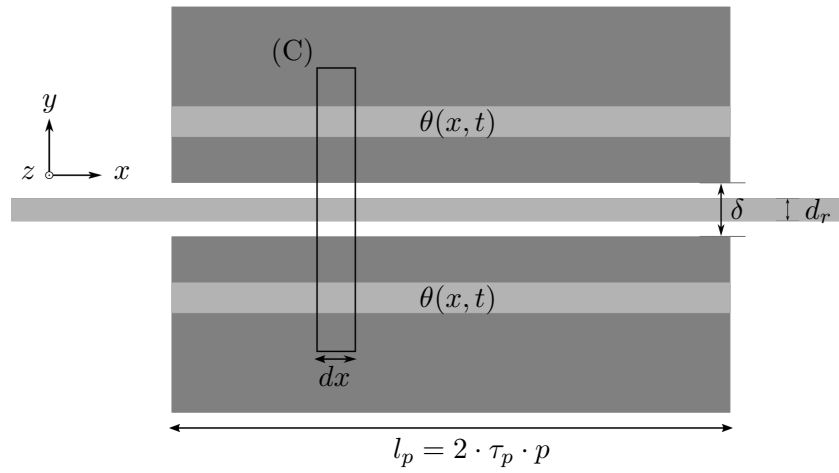

Figure 2.2: Schematic of a DSLIM with the closed curve (C) and distributed MMF.

of primary sides n_p. Using $B_y = \mu_0 H_y$ yields

$$\frac{\partial}{\partial x} B_y(x,t) = \theta_{tot}(x,t) \frac{\mu_0 n_p}{\tau_p \delta} + J_z(x,t) \frac{\mu_0 d_r}{\delta} \ . \tag{2.14}$$

$J_z(x,t)$ are the currents that are inside the secondary conductor. These occurring currents are the eddy currents induced by the time-changing magnetic fields as no external electric field is in the secondary. Faraday described the connection between time-changing magnetic fields and electric fields with the law of inductance.

$$\oint_{\partial A} \mathbf{E}\, \mathrm{dl} = -\frac{\partial}{\partial t} \iint_A \mathbf{B}\, \mathrm{d}\mathbf{A} \tag{2.15}$$

Applying this to a closed curve (C1) perpendicular to the previous curve (C) inside the secondary conductor yields

$$E_z(x,t)w_s - E_z(x+dx,t)w_s = -\frac{\partial}{\partial t}\mathbf{B}(x,t)\mathbf{e}_y w_s dx \tag{2.16}$$

$$\frac{\partial}{\partial x} E_z(x,t) = \frac{\partial}{\partial t}\left[\mathbf{B}(x,t)\mathbf{e}_y\right] \tag{2.17}$$

$$\frac{\partial}{\partial x} E_z(x,t) = \left[\frac{\partial}{\partial t}B_y(x,t) + v\frac{\partial}{\partial x}B_y(x,t)\right] \ , \tag{2.18}$$

where w_s is the depth of the model and therefore the dimension in z-direction of the LIM. The second term in the time derivative of the magnetic field in (2.18) is because the loop is considered as fixed on the secondary conductor. So if the motor is moving the change of position will introduce a change in magnetic field. With the current density defined as

$$\mathbf{J}(x,t) = \sigma_s \mathbf{E}(x,t) \ , \tag{2.19}$$

equation (2.18) and the derivative of (2.14) result in

$$\frac{\partial^2}{\partial x^2}B_y(x,t) - \frac{\sigma_s \mu_0 d_r}{\delta}\left[\frac{\partial}{\partial t}B_y(x,t) + v\frac{\partial}{\partial x}B_y(x,t)\right] = \frac{\mu_0 n_p}{\tau_p \delta}\frac{\partial}{\partial x}\theta_{tot}(x,t) \ . \tag{2.20}$$

The magnetic field $B_y(x,t)$ is generated by $\theta_{tot}(x,t)$ and therefore has the form

$$B_y(x,t) = B_s \mathrm{e}^{\mathrm{j}(-\omega t + \frac{\pi}{\tau_p}x + \Phi)} \tag{2.21}$$

(2.8) and (2.21) in (2.20) yields

$$-\left[\frac{\pi}{\tau_p}\right]^2 B_y(x,t) - \frac{\sigma_s \mu_0 d_r}{\delta}\left[-\mathrm{j}\omega B_y(x,t) + \mathrm{j}v\frac{\pi}{\tau_p}B_y(x,t)\right] = \mathrm{j}\frac{\mu_0 n_p \pi}{\delta \tau_p^2}\theta_{tot}(x,t) \tag{2.22}$$

$$\left[-\left(\frac{\pi}{\tau_p}\right)^2 + \mathrm{j}\frac{\sigma_s \mu_0 d_r \pi}{\delta \tau_p}(v_s - v)\right]B_s \mathrm{e}^{\mathrm{j}\Phi} = \mathrm{j}\frac{\mu_0 \pi}{\delta \tau_p^2}n_p\frac{3}{2}A \tag{2.23}$$

$$\left[-\left(\frac{\pi}{\tau_p}\right)^2 + \mathrm{j}\frac{\sigma_s \mu_0 d_r \pi}{\delta \tau_p}(v_s - v)\right]B_s = \frac{\mu_0 \pi}{\delta \tau_p^2}n_p\frac{3}{2}A(\sin\Phi + \mathrm{j}\cos\Phi) \ . \tag{2.24}$$

Dividing into imaginary and real parts leaves

$$-\left(\frac{\pi}{\tau_p}\right)^2 B_s = \frac{\mu_0 \pi}{\delta \tau_p^2} n_p \frac{3}{2} A \sin \Phi \qquad (2.25)$$

$$\frac{\sigma_s \mu_0 d_r \pi}{\delta \tau_p}(v_s - v)B_s = \frac{\mu_0 \pi}{\delta \tau_p^2} n_p \frac{3}{2} A \cos \Phi \ . \qquad (2.26)$$

This can further be simplified to

$$-\frac{2\pi\delta}{3n_p\mu_0} B_s = A \sin \Phi \qquad (2.27)$$

$$\frac{2\sigma_s d_r \tau_p}{3n_p}(v_s - v)B_s = A \cos \Phi \qquad (2.28)$$

and B_s and Φ can then be calculated as

$$\Phi = \arctan\left[\frac{\pi\delta}{\mu_0 \sigma_s d_r \tau_p (v - v_s)}\right] \qquad (2.29)$$

$$B_s = \frac{n_p \frac{3}{2} A}{\sqrt{\left[\frac{\pi\delta}{\mu_0}\right]^2 + (\sigma_s d_r \tau_p)^2 (v_s - v)^2}} \ . \qquad (2.30)$$

The eddy currents can then be derived from (2.18) and (2.19) as

$$J_z(x,t) = \sigma_s \left[\int \frac{\partial}{\partial t} B_y(x,t)\,dx + vB_y(x,t)\right] \qquad (2.31)$$

$$J_z(x,t) = \sigma_s(v - v_s)B_y(x,t) \qquad (2.32)$$

2.3 Lorentz Force

In the previous section the magnetic field in the air gap of a LIM and the eddy currents induced in the secondary conductor were derived. From these two the thrust generated by a linear motor can be derived using the Lorentz Force. It states that on any moving charge in an electromagnetic field the following force is applied to it.

$$\mathbf{F} = q\mathbf{E} + \mathbf{J} \times \mathbf{B} \ . \qquad (2.33)$$

No external electric field is applied to the secondary conductor and therefore only the second part of the equation is considered. For the thrust analysis only the x-component is of interest which leads to

$$f_x = J_y B_z - J_z B_y \ , \qquad (2.34)$$

where again the first term can be neglected as the current generating the B-Field is assumed to be only in z-direction and therefore $B_z = 0$. In this assumption the winding heads of the LIM are neglected. This is usually acceptable as they are kept as small as possible and therefore have a much lower impact on the behaviour of a motor. To show this negligible impact a 3D analysis using ANSYS Mawell [11] was conducted. Results are described in chapter 3.

Applying the magnetic field $B_y(x,t)$ and the current density $J_z(x,t)$ derived to Equation (2.34), the force density for a LIM can be derived. By integrating over the volume of the secondary one gets the total thrust of the motor.

$$F_{thrust} = \iiint_V \text{Re}[J_z(x,t)\,B_y^*(x,t)]dV \tag{2.35}$$

For a short secondary motor the volume is straight forward. For a short primary the length of the primary side is to be considered for the volume integral. With $J_z(x,t)$ and $B_y(x,t)$ from (2.32) and (2.21) constant over y and z it results in

$$F_{thrust} = w_s d_r l_p \sigma_s (v - v_s) B_s^2 \ , \tag{2.36}$$

where l_p is the length of the primary , d_r is the thickness of the the secondary conductor sheet and w_s is the dimension of the LIM in z-direction. The behaviour of thrust to speed when changing different parameters is shown in Fig. 2.3. This behaviour corresponds closely to the one described in the theory of asynchronous rotary machines [12].
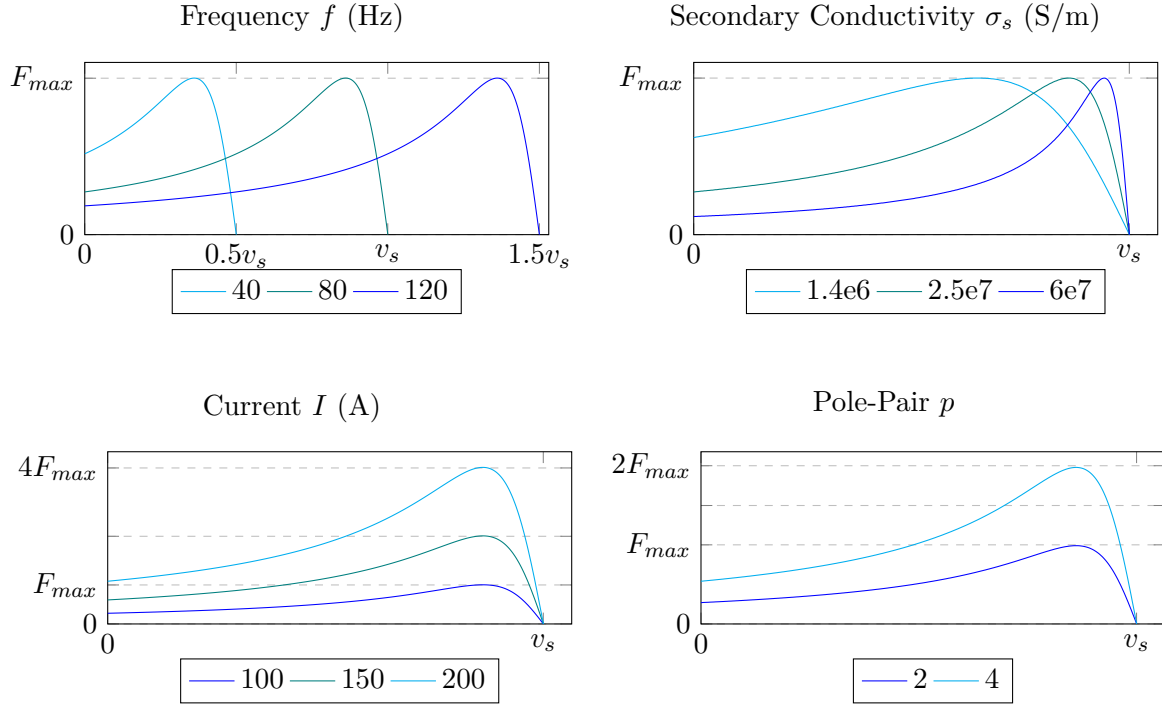

Figure 2.3: Behaviour of the thrust when changing different parameters.

2.4 Reducing Harmonics

Up until now only the first harmonic has been discussed. Higher harmonics have a smaller pole-pitch due to the higher spatial frequency. With a smaller pole-pitch the respective synchronous frequency decreases. This results in a negative slip for higher harmonics most of the time

which means they are in generator mode and therefore reduce the thrust of the motor. By introducing a Fractional Slot Concentrated Winding (FSCW) the 5th and 7th harmonic of the Slot Concentrated Winding (SCW) for LIM20 can nearly be crossed out (Fig. 2.4). However, an optimization showed that the thrust to weight ratio was higher for the SCW and therefore this design was chosen for the LIM20. Due to the quadratic behavior of the thrust to the amplitude the effects of higher harmonics were smaller than expected. Along with this, the production of FSCW proved to be complicated, which resulted in a heavier design.
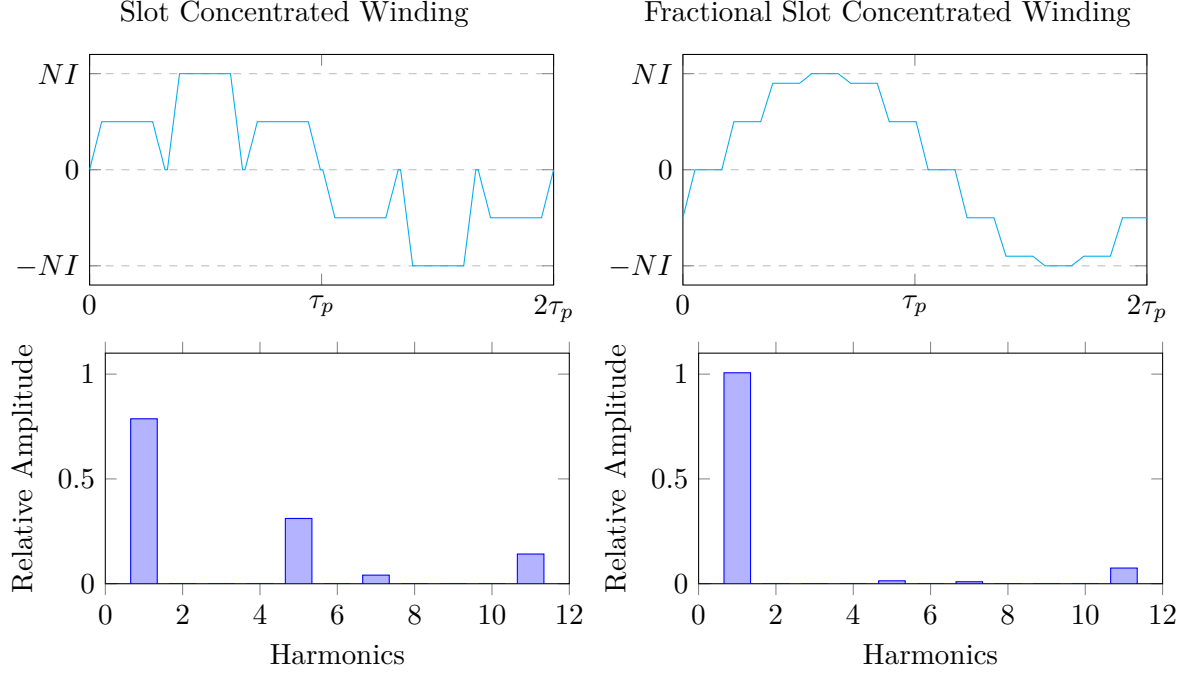

Figure 2.4: The MMF and its harmonic analysis of the SCW of the LIM20 and a FSCW.

2.5 End-Effects

By looking at Equation (2.20) the general solution of this equation has the form

$$B_y(x,t) = B_s e^{j(-\omega t + \frac{\pi}{\tau_p}x + \Phi)} + B_1 e^{\frac{-x}{\alpha_1}} e^{j(\omega t - \frac{\pi}{\tau_1}x)} + B_2 e^{\frac{x}{\alpha_2}} e^{j(\omega t + \frac{\pi}{\tau_1}x)} \ , \tag{2.37}$$

where α_1 and α_2 are both positive factors dependent on the speed of the LIM. The second term (B_1-wave) is a forward traveling wave and the third term (B_2-wave) is a backward traveling wave. Both waves propagate with the same speed and decay while traveling, their distance of penetration is given by α_1 and α_2 [5]. These terms are called the end-effects. The second term is called the entry-end-effect and the third term the exit-end-effect, in respect to where they occur. The magnitude of the end-effects are constants given by the two boundary conditions[5],

$$\int_0^{l_s} B(x,t)\,dx = 0 \tag{2.38}$$

and

$$B(0,t) = -\frac{\rho_s}{v} J_{primary}(0,t) \ . \tag{2.39}$$

It can be shown that the exit-end-effects decay very quickly and have a minor effect on the behavior of the LIM. The entry-end-effects however gain importance at higher speeds. At very high speeds B_1 almost neutralizes the normal wave B_s near the entry end which results in a large reduction of thrust.

The two end-effects can be imagined as field and energy left behind at the end of the LIM and the need of energy to constantly induce eddy currents to new secondary conductive material that comes into the LIM.

For high-speed applications like the Hyperloop, these end-effects play an important part in designing the LIM. A rule of thumb thereby is "the more pole-pairs the better". This can also be seen in the simulations shown later.

3 Thrust

Initially, Swissloop designed a 6 pole-pair LIM to take to the SpaceX Hyperloop Pod Competition 2020. In January 2020 the competition was canceled and Swissloop decided to produce only a smaller variant of this LIM with one pole-pair to verify and test the idea of the SDLIM. This smaller LIM is called the "BabyLIM".

Figure 3.1: The two primary sides of the BabyLIM.

Variables	d_r	δ	τ_p	d_t	d_w	w_s	p	N	I_{peak}
Value	10.4 mm	20.4 mm	96.3 mm	20 mm	12.1 mm	53.2 mm	1	56	150 A

Table 3.1: Dimensions of the BabyLIM.

3.1 1D Analysis in Python

The theory of chapter 2 was implemented using Python. The full script can be seen in Appendix A.1. As no geometrical aspects as the shape of the teeth and winding windows have been taken into account it must be taken with caution. These geometries highly affect the shape of the curve. However, this analysis can be conducted to get a first impression on how the motor thrust will behave and in what range the thrust can be expected.

The result of this analysis for a one pole-pair LIM with a primary frequency of 40 Hz, 80 Hz and 120 Hz is shown in Fig. 3.2. It can be seen that the curve stays the same but gets shifted to the right with increasing frequency. The BabyLIM shows the expected behaviour with a maximum thrust of about 850 N. Looking at the LIM20 with 6 pole-pairs a maximum thrust of 5100 N is observed (Fig. 3.3). Except for the maximum thrust, the shape of the curve does not

change with increasing pole-pairs. Further simulations will show under what circumstances these results can be a legitimate approximation.
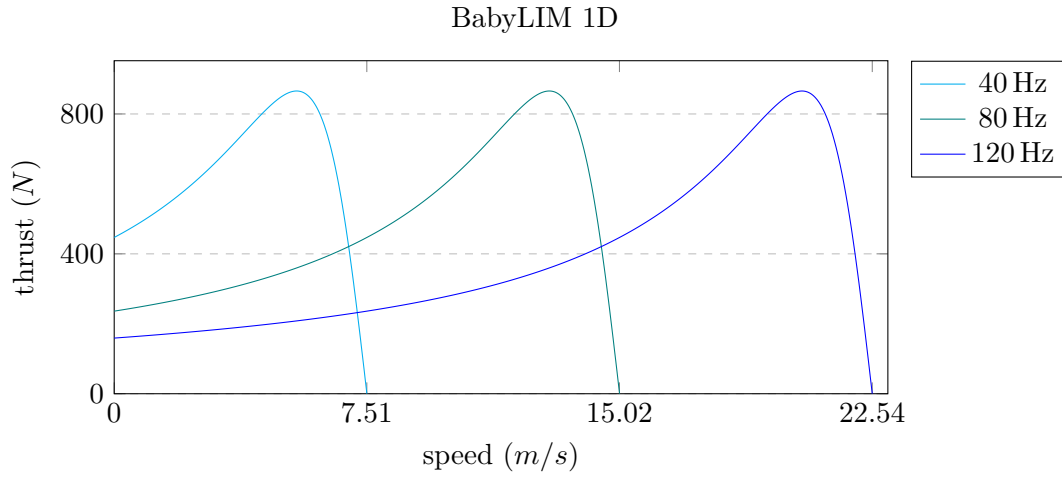
BabyLIM 1D

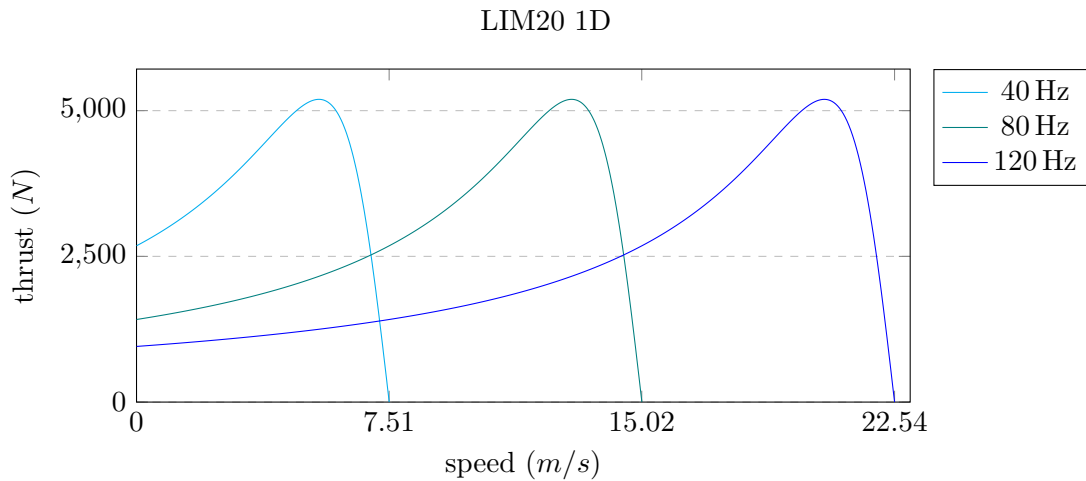Figure 3.2: 1D Thrust-Speed analysis of the BabyLIM.

LIM20 1D

Figure 3.3: 1D Thrust-Speed analysis of the 6 pole-pair LIM20.

3.2 2D Simulation with ANSYS Maxwell

To get more accurate results and verify the 1D analysis a 2D simulation using ANSYS Maxwell is conducted. In addition to the aspects of the 1D analysis, Finite Element Method (FEM) simulations done with such a program take multiple additional effects into account. The geometry includes the shapes of teeth and winding windows as well as the overall height. The iron is taken as a metal with a defined B-H-curve that is given by the material of the

manufacturer. With it saturation effects of this material core can be seen. Additionally to the saturation, End-effects are taken into account in such an analysis. End-effects will prove to have the biggest impact on the behavior of the BabyLIM.

3.2.1 BabyLIM

The model for the simulation was drawn in ANSYS Maxwell with the dimensions given in Table 3.1. To simplify the design and speed up the computation a symmetry axis was introduced in the middle of the secondary aluminum conductor. This symmetry is defined as an even symmetry which means that the flux is normal to it. The model was designed to be as close as possible to the real DSLIM and therefore the curved edge at the top and the cuts for the security plates in the teeth were also modeled. The impact of those elements on the result have been proven to be negligible but as they did not affect the computation time they were kept in the model. The coils are modeled as two plane copper sheets and defined as stranded. This means that no eddy currents are calculated in the copper sheet and the current is evenly distributed over the area. With a wire area of $3\,\text{mm}^2$ in the original coils and a maximum frequency of $1\,\text{kHz}$, the penetration depth of the skin effect is $2\,\text{mm}$. Therefore this simplification can be done. For the mesh size a maximum of $6\,\text{mm}$ was chosen. A screenshot of the model in ANSYS Maxwell is given in Fig. 3.4.
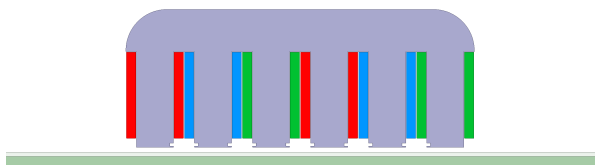

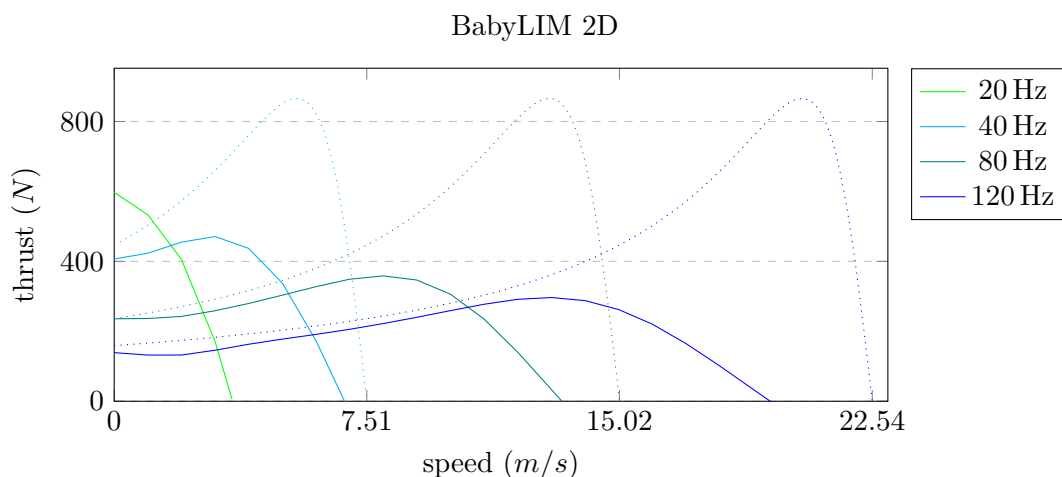Figure 3.4: 2D model of the BabyLIM in ANSYS Maxwell.

Figure 3.5: Comparison of the BabyLIM 2D simulation with the 1D analysis (dotted).

The transient electromagnetic analysis was done using a parametric setup to sweep the speed from $0\,\mathrm{m\,s^{-1}}$ to $25\,\mathrm{m\,s^{-1}}$ in steps of $1\,\mathrm{m\,s^{-1}}$. The simulation time was chosen to be $80\,\mathrm{ms}$. To account for the settling of the motor the results were then averaged between 40-80 ms. Fig. 3.5 shows the thrust-speed characteristic of the BabyLIM simulated with the model in Fig. 3.4.

The results obtained in these simulations show a big difference to the results of the 1D analysis when getting to a low slip. This is mostly due to the end-effects, as those are the only effects that differ with speed. This also shows, that the effect of higher harmonics on the thrust are comparably small.
It takes about one pole-pair to fully induce the field in the secondary [5]. This means that with more pole-pairs the end-effects would get smaller compared to the overall force. Therefore, it makes sense to check if the end-effects are equally serious in the full 6 pole-pair LIM20.

3.2.2 LIM20

The DSLIM Swissloop designed for its season 2019/2020 has 6 pole-pairs. The other parameters are the same as for the BabyLIM and are given in Table 3.1. The 2D model has been drawn with the same simplifications as stated above for the BabyLIM and is shown in Fig. 3.6.
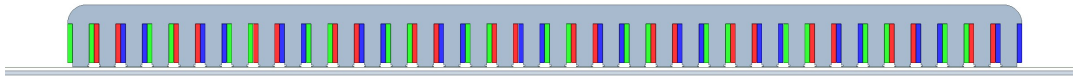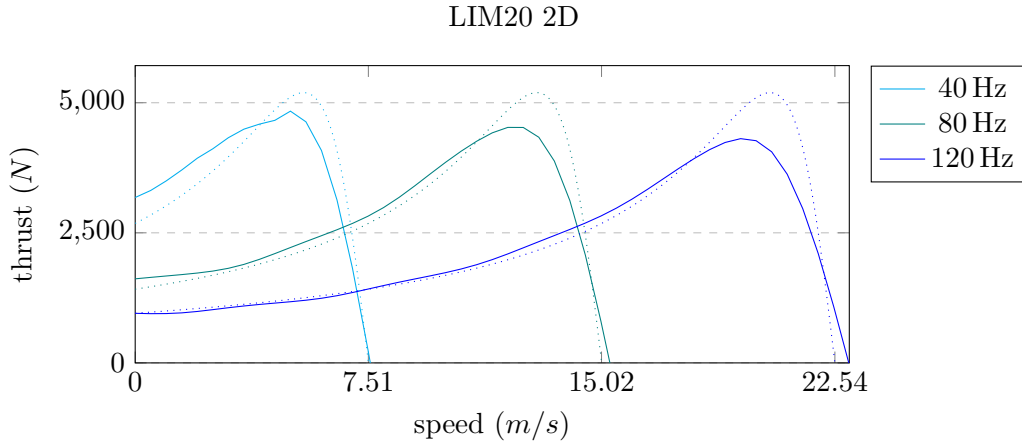

Figure 3.6: 2D model in ANSYS Maxwell for the LIM20.

Figure 3.7: Thrust of the LIM20 2D simulation compared to the 1D analysis (dotted).

The result of this analysis with a frequency f_p of $40\,\mathrm{Hz}$, $80\,\mathrm{Hz}$ and $120\,\mathrm{Hz}$ are calculated in the same manner as for the BabyLIM and are presented in Fig. 3.7. Comparing the results to those of the 1D analysis shows a close match between them. The impact of the end-effects is much smaller than on the BabyLIM. This is the expected behavior and shows that longer LIM

with multiple pole-pairs are better suited for high-speed applications. Nevertheless, end-effects still have a great impact and the maximum thrust falls below $2\,\mathrm{kN}$ for speeds above $140\,\mathrm{m\,s^{-1}}$ ($540\,\mathrm{km\,h^{-1}}$) as shown in Fig. 3.8.
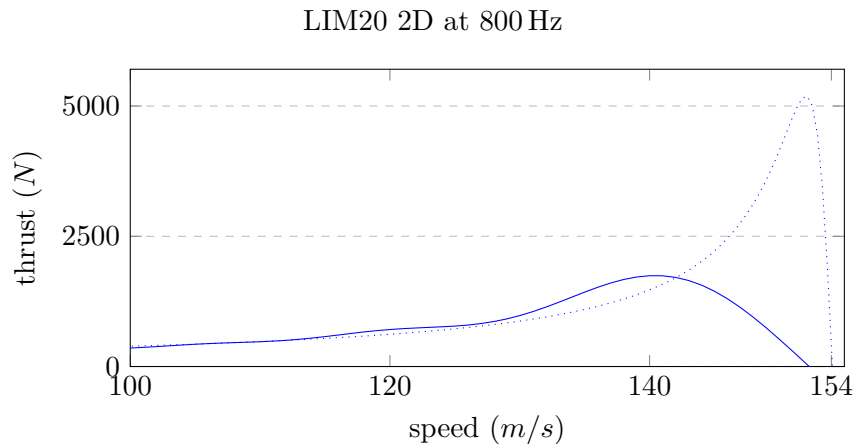

Figure 3.8: Thrust of the LIM20 2D simulation vs. 1D analysis (dotted) at $800\,\mathrm{Hz}$.

3.3 3D Simulation with ANSYS Maxwell

In a design process a 3D model should finally be applied to verify the results of the 2D model and including the winding heads. Those can not be modeled in the 2D design and in a typical rotary motor the winding heads can have a noticeable effect on the behavior of the machine. In the case of the LIM20 the overheads are comparably small and therefore the effect on the thrust is expected to be negligible. The model used for this analysis is shown in Fig. 3.9.
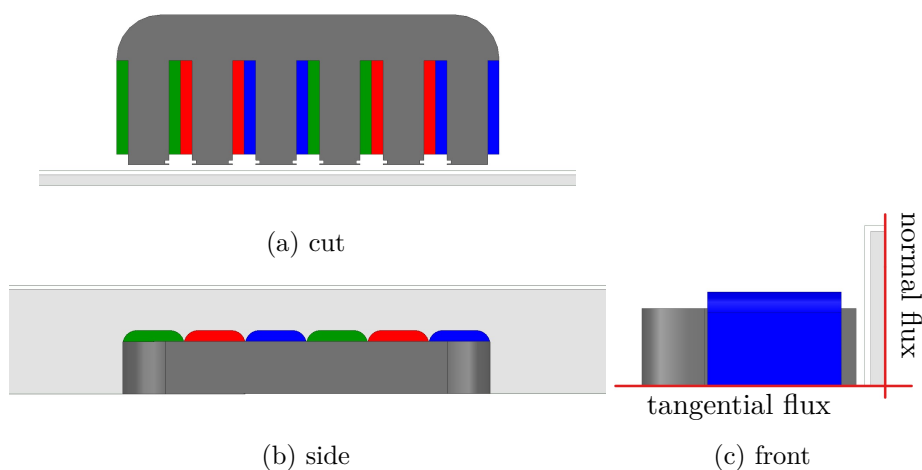

(a) cut

(b) side

(c) front

Figure 3.9: 3D model in ANSYS Maxwell for the BabyLIM with the two symmetry planes marked red in the front view.

Thrust

3D models are much more complicated than 2D models and the time it takes to simulate can quickly become more than double the time for a similar 2D model. For that reason only the BabyLIM is modeled and then compared to the results of the 2D simulation. From there, a conclusion for the LIM20 can be made. Besides the symmetry introduced in the 2D model, a second symmetry plane is introduced. This symmetry plane cuts the LIM in half and is defined as a tangential flux symmetry. So for the 3D model only one quarter of the LIM needs to be analyzed, which reduces computation time effectively. However, the simulations still take a lot longer than 2D models.
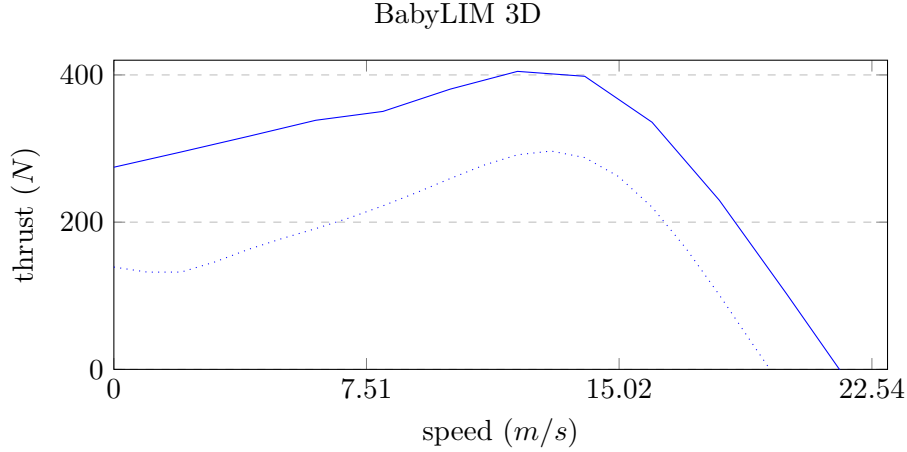
BabyLIM 3D

Figure 3.10: Thrust-speed analysis at 120 Hz, 3D simulation compared to 2D (dotted).

When comparing the results of the 3D analysis to the 2D analysis of the BabyLIM they are about 30 % higher than expected (Fig. 3.10). As the curve is just lifted it seems as if the LIM is actually longer or wider than simulated in the 2D model. This appears due to the wider actual penetration width of the aluminum sheet by leakage fields and the nonhomogeneous air gap field. When looking at the magnetic field in the core and the eddy-current in the aluminum this can be seen as the eddy-currents go beyond the dimensions of the primary (Fig. 3.13). When lowering the width of the secondary to match the width of the primary the results in Fig. 3.11 are obtained. These results look as if the conductivity of the secondary had been lowered. This is not the case. But by reducing the width the current has less place at the border to move in the circular motion. This results in higher current densities at the border or respectively higher resistance due to the smaller area. This has to be accounted for if the secondary has the exact same width as the primary.

In Swissloops case the secondary width is greater than the primary. To match the 2D design the spread of the magnetic field has to be taken into consideration. This can be done using the Schwarz-Christoffel-Transformation. With it the actual air-gap reluctance is derived as

$$R'_b = \frac{1}{\mu_0 \left[\frac{w}{2l} + \frac{2}{\pi} \left(1 + \ln \frac{\pi h}{4l} \right) \right]} \ , \tag{3.1}$$

with the structure described in Fig. 3.14 [13]. When comparing this to the air gap reluctance
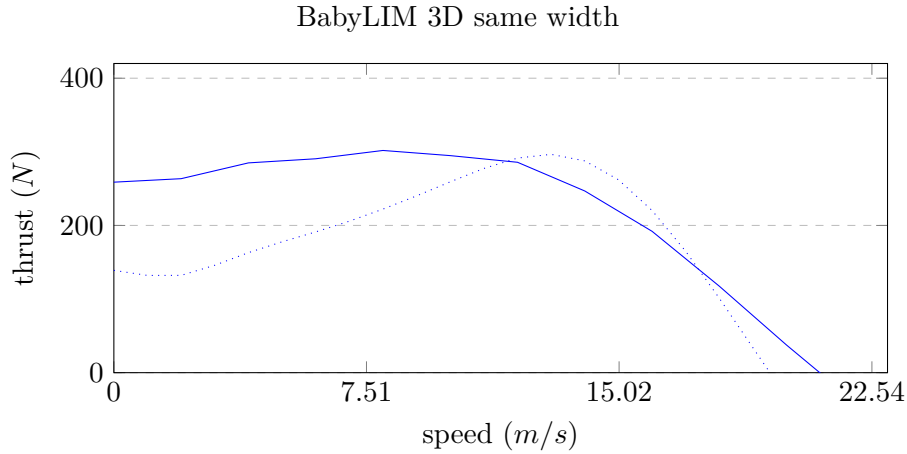
BabyLIM 3D same width

Figure 3.11: 3D compared to 2D (dotted) when matching the width of secondary and primary.

of a homogeneous field

$$R'_{m,air} \approx \frac{2l}{\mu_0 w} \ , \tag{3.2}$$

the effect of the material is widened by

$$\Delta w = \frac{\frac{w}{2l} + \frac{2}{\pi}\left(1 + \ln\frac{\pi h}{4l}\right)}{2l} \ . \tag{3.3}$$

Applying this to the 2D model and comparing the results to the 3D simulation, results in a much smaller difference. The maximum thrusts match very closely. However, at lower speeds this is still not a suitable explanation. The field produced by the winding heads has a much greater influence there then around maximum thrust. When going in a low slip region, this is again the case.

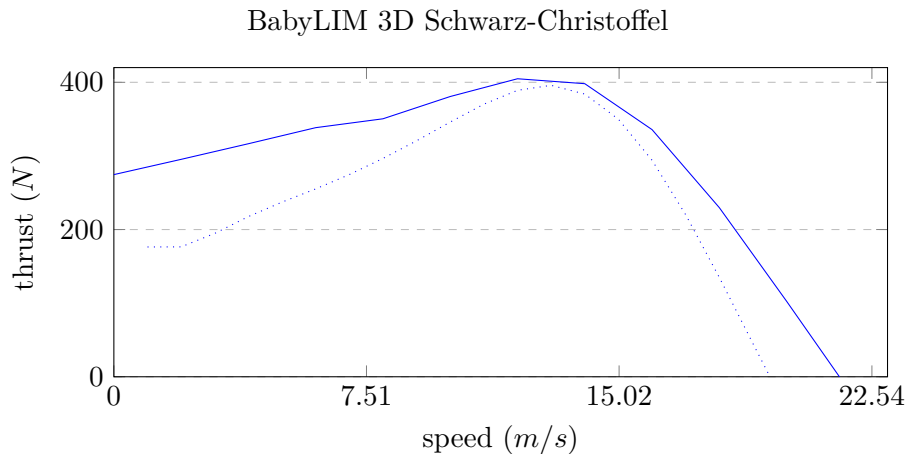BabyLIM 3D Schwarz-Christoffel

Figure 3.12: Thrust-speed analysis at 120 Hz, 3D simulation compared to 2D with Schwarz-Christoffel-Transformation (dotted).
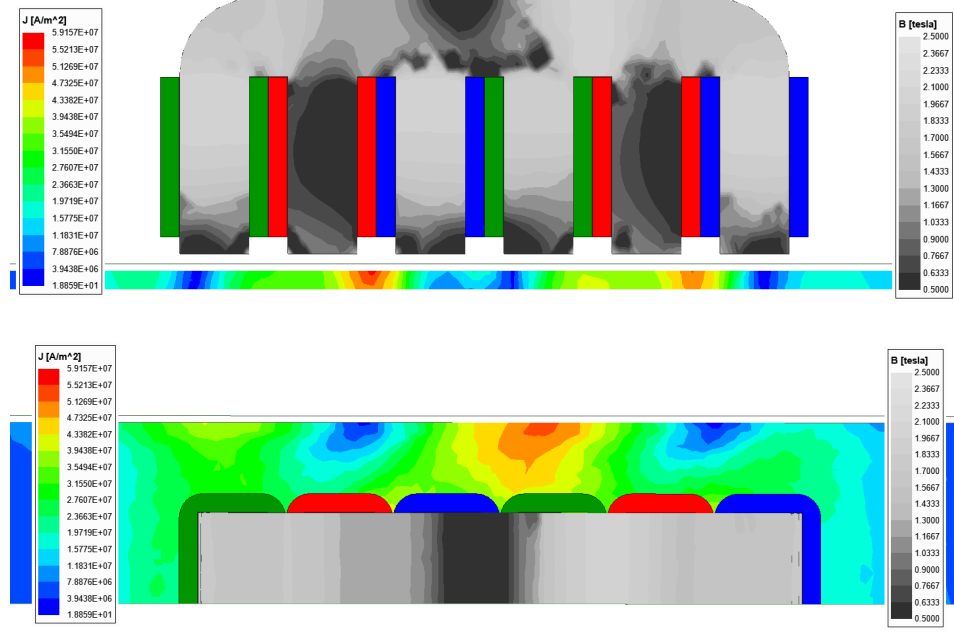
Figure 3.13: Magnitude of the magnetic field in the core and the eddy-currents in the aluminum.
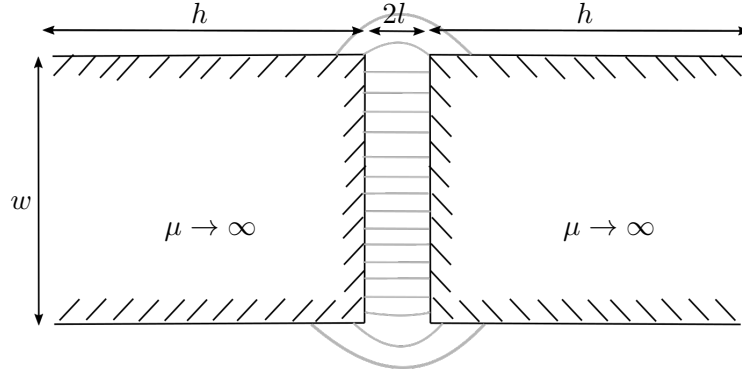

Figure 3.14: Structure for the Schwarz-Christoffel-Transformation.

3.4 Conclusion

For high pole-pair numbers the 1D analysis is a powerful tool to investigate in what region the thrust will be in a design process. However, end-effects should be included in this analysis to improve reliability. They play an important part in designing high speed LIM. For few pole-pairs their influence at low speeds is already significant. Above $7\,\mathrm{m\,s^{-1}}$ the thrust of the BabyLIM is less than $50\,\%$ of the assumed thrust of the 1D analysis. When using more pole-pairs the influence at lower speeds is comparably small but gets again significant as soon as higher speeds are reached. Investigations to lower the end-effects must be made if high thrust is needed at high speeds.

In 2D simulations the depth of the model has to be carefully set. For accurate results the

three-dimensional picture needs to be known. From there more accurate solutions can be simulated with the Schwarz-Christoffel-Transformation. For the BabyLIM with the Schwarz-Christoffel-Transformation this results in the expected thrust curves as shown in Fig. 3.15. However, they are expected to match the real data only on the maximum thrust points of every curve, because of the influence of the winding heads.

Due to the long simulation times for 3D models it is not recommended to use them in an early design phase. See section 6.1 for more details. However, for final results a 3D simulation at critical points should be considered.
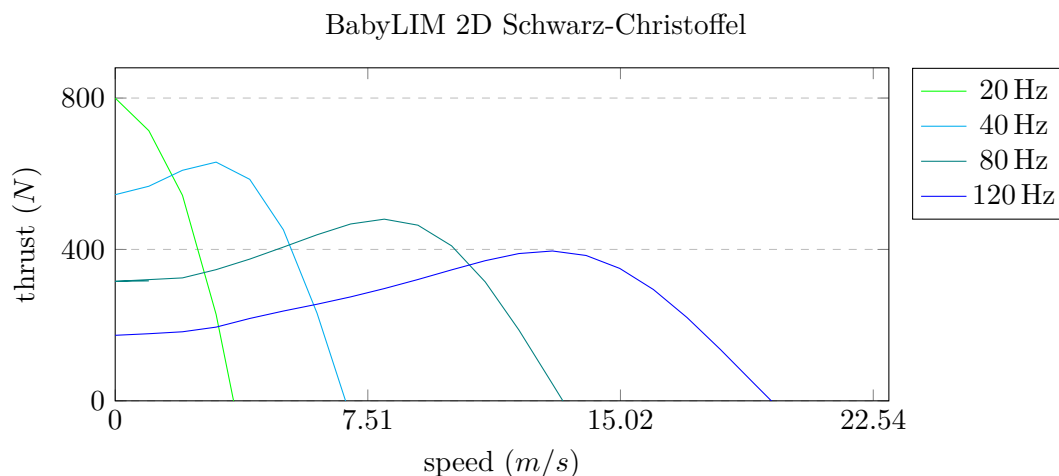

Figure 3.15: 2D simulation of the BabyLIM using Schwarz-Christoffel.

4 Pole-Pitch Transition

When designing vehicles for high-speed applications like Hyperloop a second challenge occurs besides the loss of thrust though by end-effects. For higher speeds higher frequencies are needed for the motor to stay in motor-mode ($0 < s < 1$) and not to slow down. With increasing frequency the supply voltage needed to drive the current rises. In Hyperloop pods with the active part on board, the energy to drive the system needs to be carried with it because of the high speeds. For electricity this is conventionally done with batteries. For "Claude Nicollier" Swissloop had a battery of $900\,\mathrm{V}$ on board [14]. This voltage maximum was quickly exploited. To further increase the frequency the current had to be reduced. According to Equation (2.36) in chapter 2 the thrust is proportional to the square of the current but is linear to the number of poles. Therefore, the idea of changing the number of poles when hitting the maximum voltage reduces the thrust only linearly compared to the quadratic reduction when lowering the current. This comes with various challenges. First of all a LIM is required where every coil can be controlled independently and an inverter that is capable of controlling multiple phases. Additionally, the now parallel structure of the windings, rather than a series connection as in the previous year, ask for a battery delivering high currents. With the LIM20, the newly designed scalable high-power multi-phase variable frequency inverter [8] and a custom-designed battery [14] made this possible.

This chapter will now investigate the current transition that is needed to do such a change in pole-pairs (or pole-pitch). Later, a 2D simulation is conducted to show how the thrust is effected by a pole-pitch transition.

4.1 Current Transition

To change the pole-pitch the speed of the second field has to match the speed of the first field in order to ensure a smooth transition. This yields

$$2\tau_1 f_1 = v_s = 2\tau_2 f_2 \tag{4.1}$$

$$\frac{f_1}{f_2} = \frac{\tau_2}{\tau_1} = \frac{p_1}{p_2} \tag{4.2}$$

when using all windings before and after the transition. Therefore, the pole-pitch needs to be doubled if the frequency is to be cut in half. With this in mind let's now look at the LIM20 from Swissloop. The LIM has 36 individually controllable phases. To now get a 6 pole-pair LIM each current must have an angle shift φ of

$$\varphi = \frac{6 \cdot 2\pi}{36} = \frac{\pi}{3} \ . \tag{4.3}$$

Because $sin(\frac{\pi}{3}) = -sin(\frac{4\pi}{3})$ this can be divided in three individual phases that are needed to drive the motor. This means with 6 pole-pairs this motor behaves as if it were driven by a three-phase current source. If now an arbitrary number of pole-pairs p are to be injected, it

results in

$$\varphi = \frac{2\pi\, p}{36} = \frac{\pi\, p}{18} \; . \tag{4.4}$$

Up to 18 pole-pairs are possible with 36 phases. Such high pole-pair numbers will however lead to a high-harmonic distorted MMF distribution, which greatly affects the efficiency of the machine. The LIM20 was designed and optimized for a 6 pole-pair topology. Hence this is assumed to be the initial state. The angle shifts φ for pole-pairs $p \leq 6$ can then be derived according to (4.4) and are listed in Table 4.1 and the corresponding current vectors for pole-pairs 6,5,4 and 3 are given in Fig. 4.1.

p	6	5	4	3	2	1
φ	60°	50°	40°	30°	20°	10°

Table 4.1: Angle shifts between phases for different pole-pairs.

These calculations above were done for a steady-state. The idea to get now from one steady-state into the other is to leave the old magnetic field behind and introduce the new field from the front. When setting the frequencies according to Equation (4.2), the fields move with the same speed and a transition can be done at the same current value for every phase.

Let's look at a pole-pitch transition from p_1 to p_2 and the transition start time t_1. This results in a current in coil 1 of

$$i_1(t_1) = I_{peak} \sin\left[2\pi f_1 t_1\right] \; . \tag{4.5}$$

To fulfill the condition that the current at time t_1 equals i_1, the current i_1' for p_2 pole-pairs must be

$$i_1'(t) = I_{peak} \sin\left[2\pi f_2(t - (f_2 - f_1)t_1)\right] \; . \tag{4.6}$$

The transition of the phase k will then be at time

$$t_k = t_1 + (k-1)\frac{p_1}{f_1 36} = t_1 + (k-1)k\frac{p_2}{f_2 36} \; , \tag{4.7}$$

with the current for phase k defined as

$$i_k(t) = I_{peak} \sin\left[2\pi f_1 t - (k-1)\frac{\pi p_1}{18}\right] \tag{4.8}$$

$$i_k'(t) = I_{peak} \sin\left[2\pi f_2(t - (f_2 - f_1)t_1) - (k-1)\frac{\pi p_2}{18}\right] \; . \tag{4.9}$$

The total transition will take $T = p_1/f_1 = p_2/f_2$ seconds. For the inverter and the control loop voltage jumps are not desired because of parasitic capacitances. Hence, for a smooth transition not only $i_k(t_k) = i_k'(t_k)$ must hold, but also

$$\frac{d\, i_k}{dt}(t_k) = \frac{d\, i_k'}{dt}(t_k) \; . \tag{4.10}$$

This is the case for $t_1 = \frac{T_1}{4} + n\, T_1$ with $n \in \mathbb{N}$ and $T_1 = \frac{1}{f_1}$, which results in $i_k(t_k) = \pm I_{peak}$. The MMF of a transition from 6 to 3 pole-pair with $i_k(t_k) = I_{peak}$ at times t_1, t_{12}, t_{24} and t_{36} is shown in Fig. 4.2.

(a) $p = 6$

(b) $p = 5$

(c) $p = 4$

(d) $p = 3$
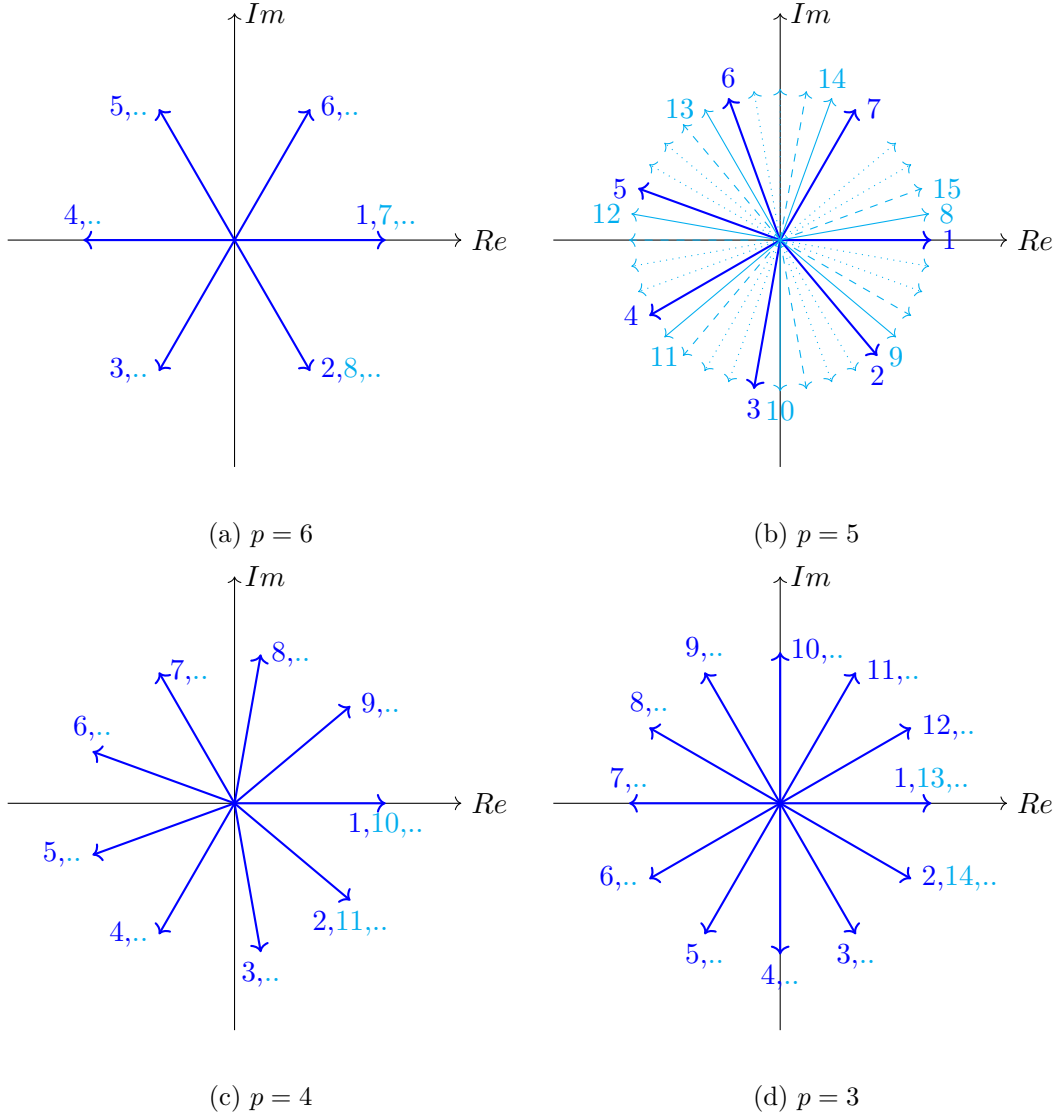
Figure 4.1: Current phases for different pole-pairs for the LIM20.
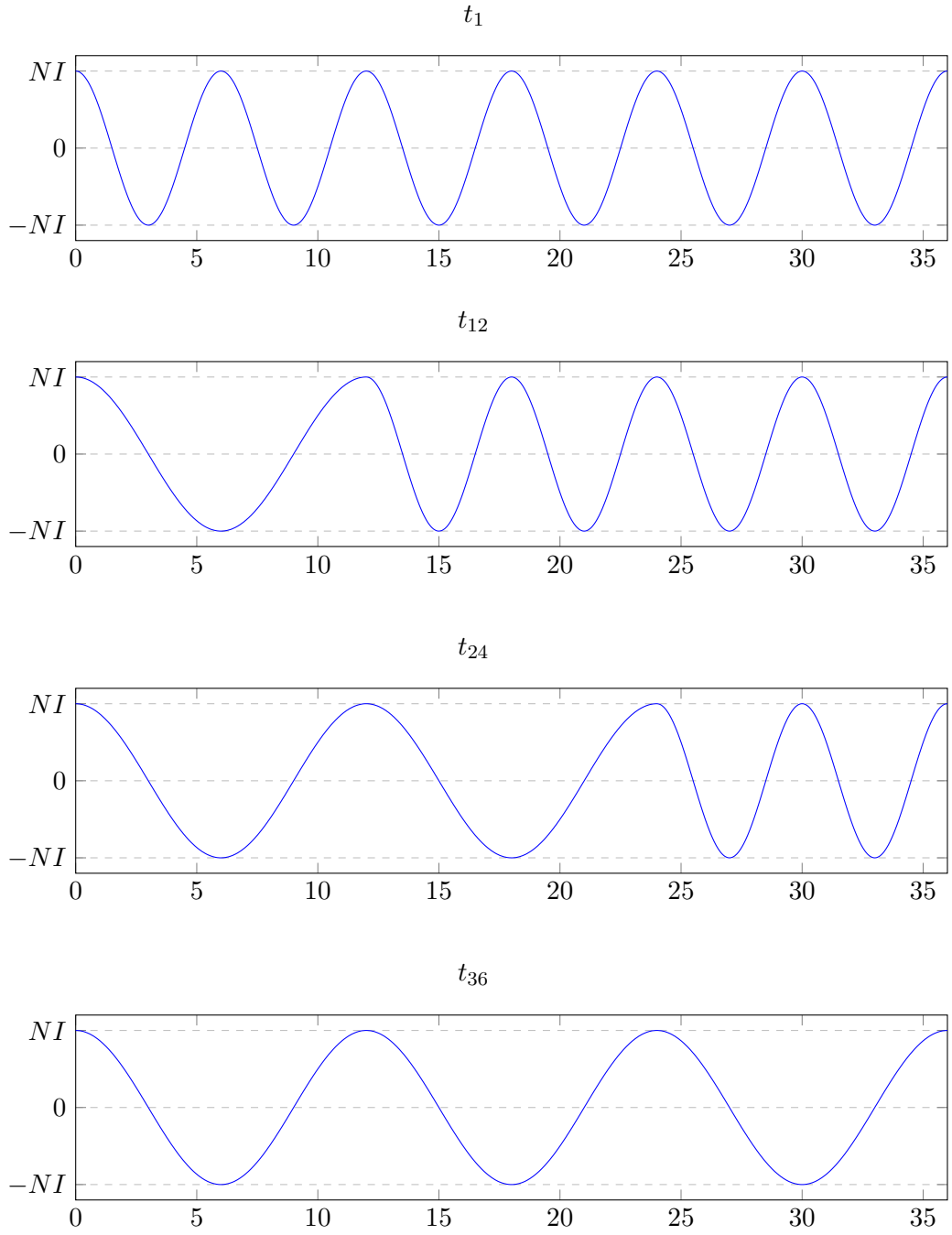
t_1

t_{12}

t_{24}

t_{36}

Figure 4.2: MMF of a pole-pitch transition from 6 to 3 pole-pair while the x-axis is the length of the LIM indicated by the number of the phase at that point.

4.2 2D Simulations with ANSYS Maxwell

To investigate the impact of such a pole-pitch transition on the thrust force a 2D simulation is conducted using ANSYS Maxwell. The behavior of the motor during the transition, when an odd number of poles are induced, is of main interest. For the simulation the 2D model of the LIM20 used previously was taken and abbreviated for this purpose. Some small changes in the definition of the copper sheets had to be made. The most important change however was the current source. Until now the windings were directly defined with a sinusoidal current in the modeler of ANSYS Maxwell. For the pole-pitch transition the frequency needed to be switchable and therefore the excitation had to be done differently. ANSYS Electronics Desktop provides a solution for more complicated current forms with Maxwell Circuits. There a circuit can easily be drawn with the windings in the model defined as inductors. The model can then be linked to this circuit where the names of the windings have to match the names of the inductors. This was done for the pole-pitch transition. By using multiple current sources and controllable switches the desired currents could be generated. The circuit design for each coil is shown in Fig. 4.3. Parallel switches to the current sources were needed to give the current a path to run when the connecting switches are off. To ensure equivalent switching the parallel switches are controlled by the inverse signal of the corresponding connecting switch.
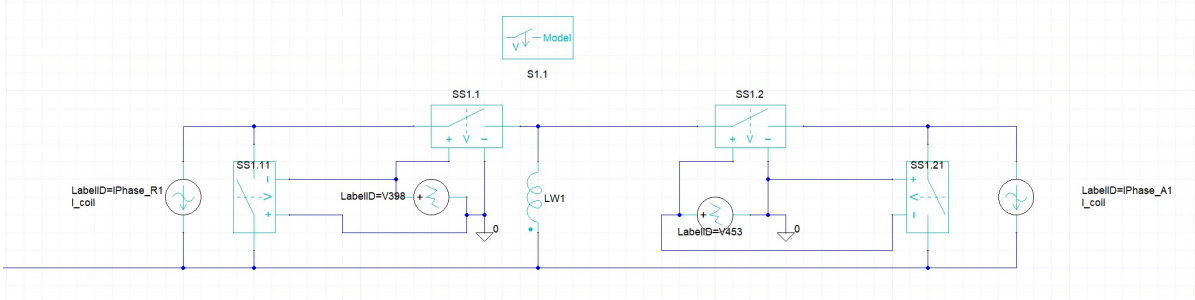

Figure 4.3: Circuit for one coil.

Simulations were then done for doubling the pole-pitch (from 6 to 3 pole-pairs) and for a transition from 6 to 5 pole-pairs which corresponds to lengthening the pole-pitch by a factor of 1.2. The simulation was started with the results from the 2D analysis of LIM20. This allowed the transition to start from a steady-state while keeping the simulation time reasonable.

4.2.1 Ideal Transition

Following the steps explained in section 4.1 the current transition was set to take place at a maximum current in every coil. This resulted in a smooth transition without an overshoot and voltage spikes, as shown in Fig. 4.4. Hereby the induced voltage could be reduced by 40 % while still maintaining over 80 % of thrust for a transition from 6 to 5 pole-pairs. If a similar reduction in voltage is to be achieved by lowering the current, one would need to go below 100 A peak current, simulations showed. This would result in a thrust of less than 2 kN, far less than with a pole-pitch-transition.

LIM20 ideal Pole-Pitch-Transition

Thrust

(a) Thrust over time

Induced Voltage
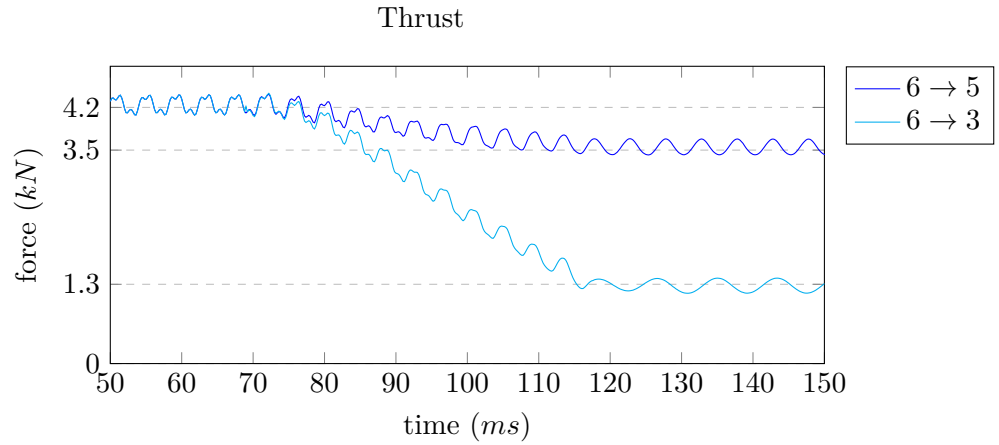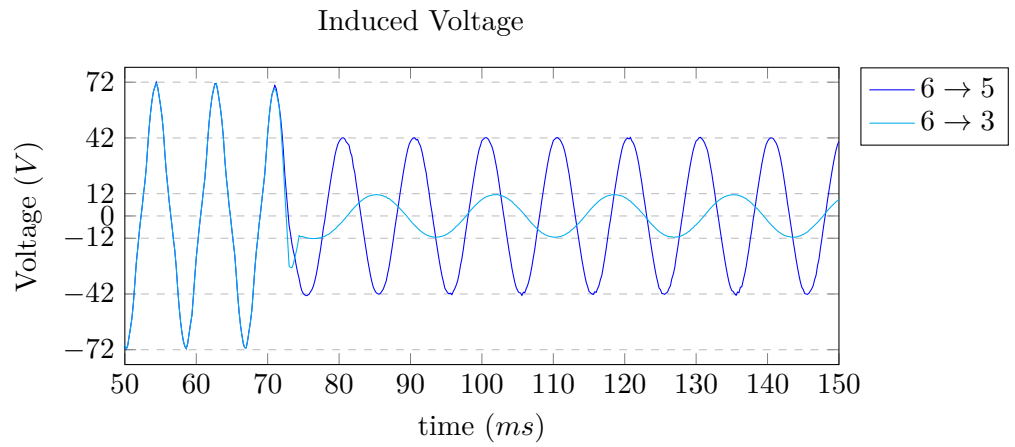
(b) Voltage over time for one winding

Figure 4.4: Ideal pole-pitch-transition at $20\,\mathrm{m\,s^{-1}}$ and $120\,\mathrm{Hz}$ starting frequency. The curves are indicated with the respective pole-pairs.

4.2.2 Non-Ideal Transition

In a non-ideal switching at least one of the two conditions is not fulfilled. First a transition is considered with unequal derivatives but the same value at the switching point and then transition points at which the current value and the derivative are non-identical.

For the first case the results are shown in Fig. 4.5. As a transition time, $t_1 = 8\,T$ was chosen, resulting in a current $i_k(t_k) = 0$. The thrust curves show a similar behavior as for the ideal transition with no overshoot. Therefore, in therms of thrust it can be seen as a smooth transition with no transient swings. However when looking at the induced voltage this changes. The two curves show a big difference in voltage behavior. For the transition from 6 to 5 pole-pairs it is almost the same as in the ideal case. There the difference in the derivative is small and has therefore only a negligible effect. If however a noticeable difference in the derivative occurs as it is the case for the transition from 6 to 3 pole-pairs, voltage jumps can be observed.

Secondly, if the current values are non-identical at the time of switching, the current through an inductor has to change quickly. This results in very high voltages as observable in the high voltage spikes in both transitions in Fig. 4.6. Contrary to expectations, this did not lead to a considerable transient swing in the thrust curve. A small overshoot can be seen in the transition and the disturbances got bigger but stayed in a manageable margin.

4.3 Convergence

The simulations for a pole-pitch transition proved to be quite challenging. For certain speeds the solver converged, at other speeds strange behavior was observed with multiple spikes in the curve and massive swings. After eliminating the already encountered design errors like a to short space to move for the aluminum secondary etc., it seemed as if the solver ran into convergence issues. This can happen as very high current densities are observed in the secondary. The initial conditions for every setup were 0 in all points. This is not optimal and in these cases it seemed as if no stable solution could be found. However, by starting already close to the solution this problem can be solved. For these simulations this could be done by starting from a converged solution that is close, for example to start from the solution of $20\,\mathrm{m\,s^{-1}}$ and calculating the solution for $19\,\mathrm{m\,s^{-1}}$.

4.4 Conclusion

At the SpaceX Hyperloop Pod Competition 2019 Swissloop hit the maximum voltage quite early in the run. They had to reduce the current to further increase the frequency and lost a lot of thrust on the way. These simulations showed that a pole-pitch-transition is a great alternative to reduce the induced voltage, while losing less thrust than with a comparable decrease in current. On the other hand, the steps are defined and it can not be done continuously. With fewer pole-pairs, the end-effect gain on influence and the reduction of thrust can no longer be approximated as linear when going below 4 pole-pairs.
When conducting a pole-pair-transition it should be controlled carefully. Larger differences in the reference curve of the controller or its derivative at the time instant of switching to the new frequency for a coil can cause severe voltage spikes. This could lead to high stresses for the inverter or even failure.

LIM20 non-ideal Pole-Pitch-Transition

Thrust

(a) Thrust over time.

Induced Voltage
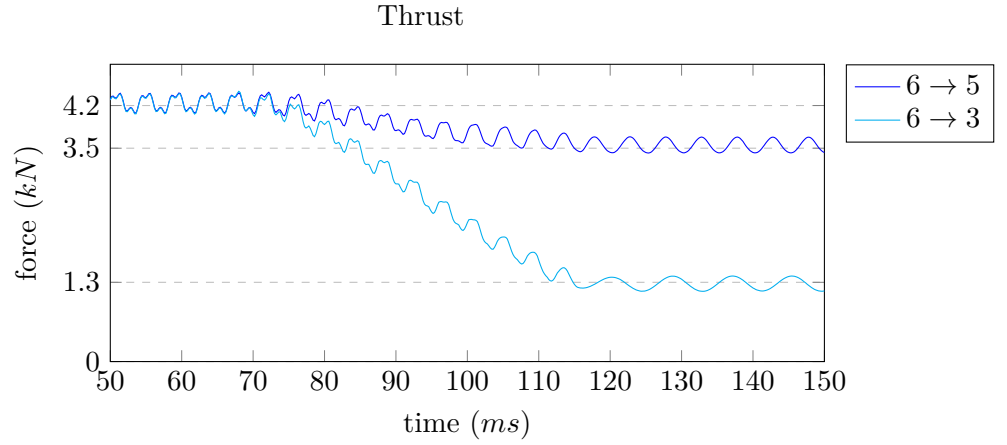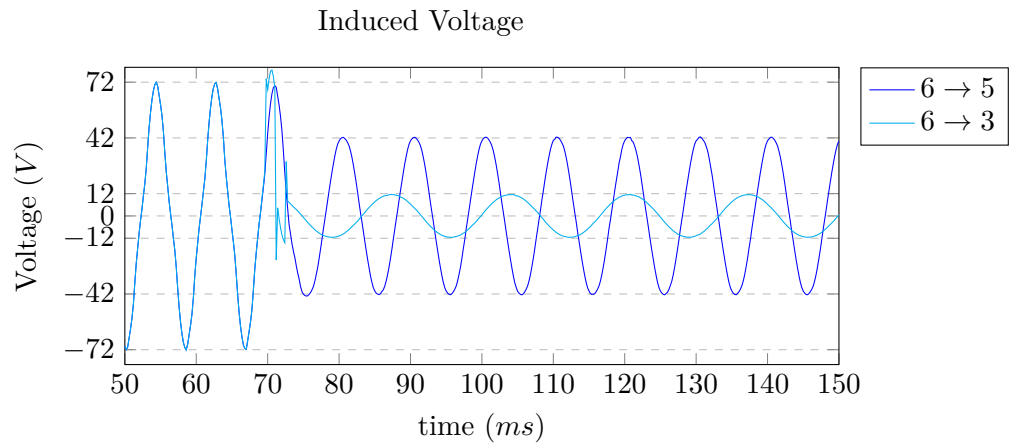
(b) Voltage over time for one winding.

Figure 4.5: Pole-pitch-transition with different derivatives at $20\,\mathrm{m\,s^{-1}}$ and $120\,\mathrm{Hz}$ starting frequency. The curves are indicated with the respective pole-pairs.

LIM20 non-ideal Pole-Pitch-Transition

Thrust

(a) Thrust over time

Induced Voltage
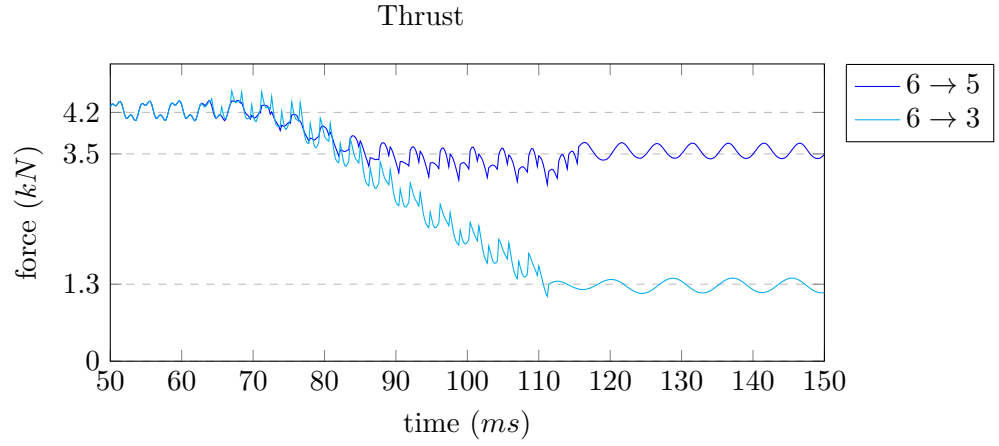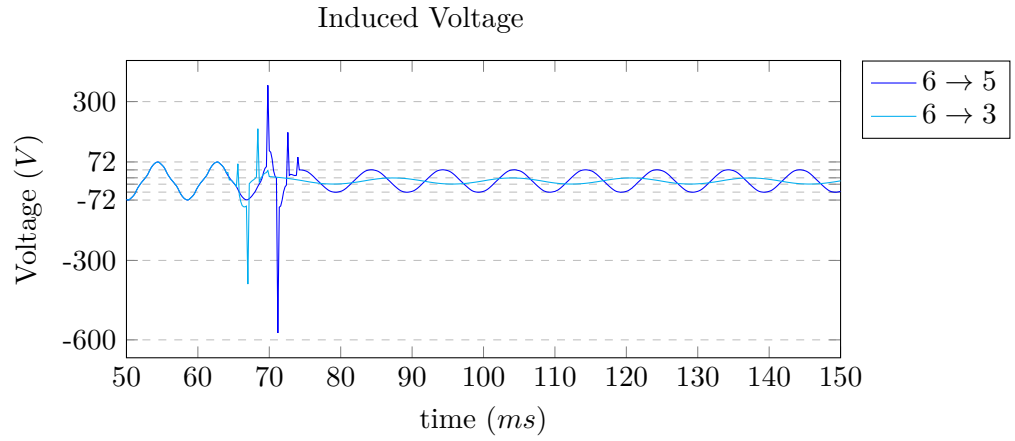
(b) Voltage over time for one winding

Figure 4.6: Pole-pitch-transition with a different value and derivatives at switching instant for $20\,\mathrm{m\,s^{-1}}$ and $120\,\mathrm{Hz}$ starting frequency. The curves are indicated with the respective pole-pairs.

5 Levitation

Swissloop's investigation of the suspension for high-speed vehicles showed multiple challenges. Up until now the suspension was done with conventional wheels and dampers. When moving fast massive forces act upon these wheels and small bumps in the track can cause deformation of them [14]. Therefore, Swissloop decided to start investigating the possibility of magnetic suspension by using the magnetic field of the LIM. Generally this can be done in two different ways. Iron could be introduced into the secondary such that the attraction force can then be used to lift the pod. Alternatively the repulsive forces of the eddy-currents in the aluminum could be used to hover above the track. Both designs are only achievable with a SSLIM. The iron in the secondary would not allow for the field to reach the primary on the other side. With a DSLIM the repulsive forces from either side are canceling each other out and levitation is not feasible.

Attraction forces to iron are much greater than the repulsive forces of the eddy-currents. For a stable system however, attraction forces should get smaller when the pod comes closer to the track and repulsive forces would need to get bigger. As both forces get bigger when the air-gap is reduced, repulsive levitation has a stabilizing effect. In this chapter the repulsive forces for a moving LIM are investigated. This is due to the track. It is a solid aluminum I-beam and only repulsive forces can, therefore, be used for suspension.

The Lorentz Force applied for levitation can be calculated from Equation (2.33). But now the component in y-direction is of interest.

$$f_y = J_z B_x - J_x B_z \tag{5.1}$$

The second term can again be neglected as we assumed the MMF to have only a z-direction and therefore $B_z = 0$. This means that the repulsion is generated by the magnetic field in the secondary in moving direction.

5.1 2D Simulations with ANSYS Maxwell

As stated above, a SSLIM will be simulated here to investigate the repulsive forces from the aluminum secondary. The DSLIM model was taken from the 2D simulations of the LIM20 and used without the symmetry plane. The thickness of the secondary was doubled and an iron backplate of the length of the primary was introduced, similar to the design in Fig. 1.1a. As the iron backplate adds weight and its distance to the primary presents a hard limit for hover width, the simulations will be done with and without it.

With an iron backplate (WI) the thrust is expected to be a quarter of the thrust of the DSLIM simulated in chapter 3. This is due to the quadratic behavior of the thrust to the MMF. When looking at the results, this is confirmed. The red curves in Fig. 5.1 shows a maximum of 1.1 kN. The design without an iron backplate (WoI) however has a much lower maximum thrust.

Without iron on the other side the field is not guided through the aluminum, which results in a lower penetration depth and therefore a lower thrust. When looking at the repelling force for levitating, a maximum of 1.3 kN is obtained for 120 Hz. The iron backplate however has not as much an influence as for the thrust. For the stable region of the motor thrust (negative derivative) the repelling force falls below 1 kN.
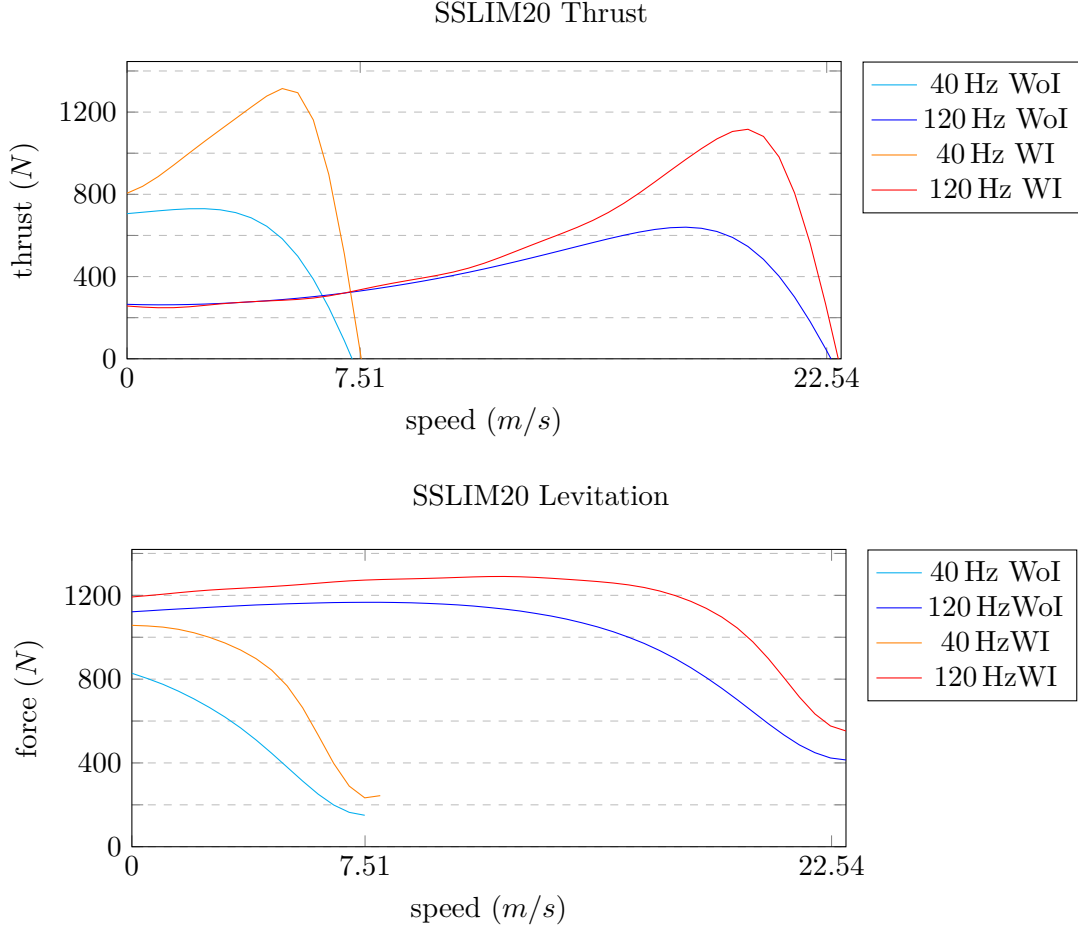

Figure 5.1: Thrust and repelling force with and without an iron backplate over speed.

With higher frequencies however a second effect takes place. Due to the frequency the current is pushed to the border of the secondary, known as skin effect. This results in high currents at the border and the field is guided through the aluminum without reaching the iron backplate. Resulting in almost no difference between the designs. In Fig. 5.2 the results of a simulation with 800 Hz are shown. On the left side of the graph a weird behavior is observed. This comes due to convergence issues of the solver. However, as this region is not of interest, and the solver converged at higher speed, they were not rectified. These speeds however could if necessary be simulated by starting with the first solution that converged and going step by step backward, always starting from the previous solution. The repelling force for 800 Hz is 1.5 kN and is again reduced when getting closer to the synchronous speed.

SSLIM20 Thrust
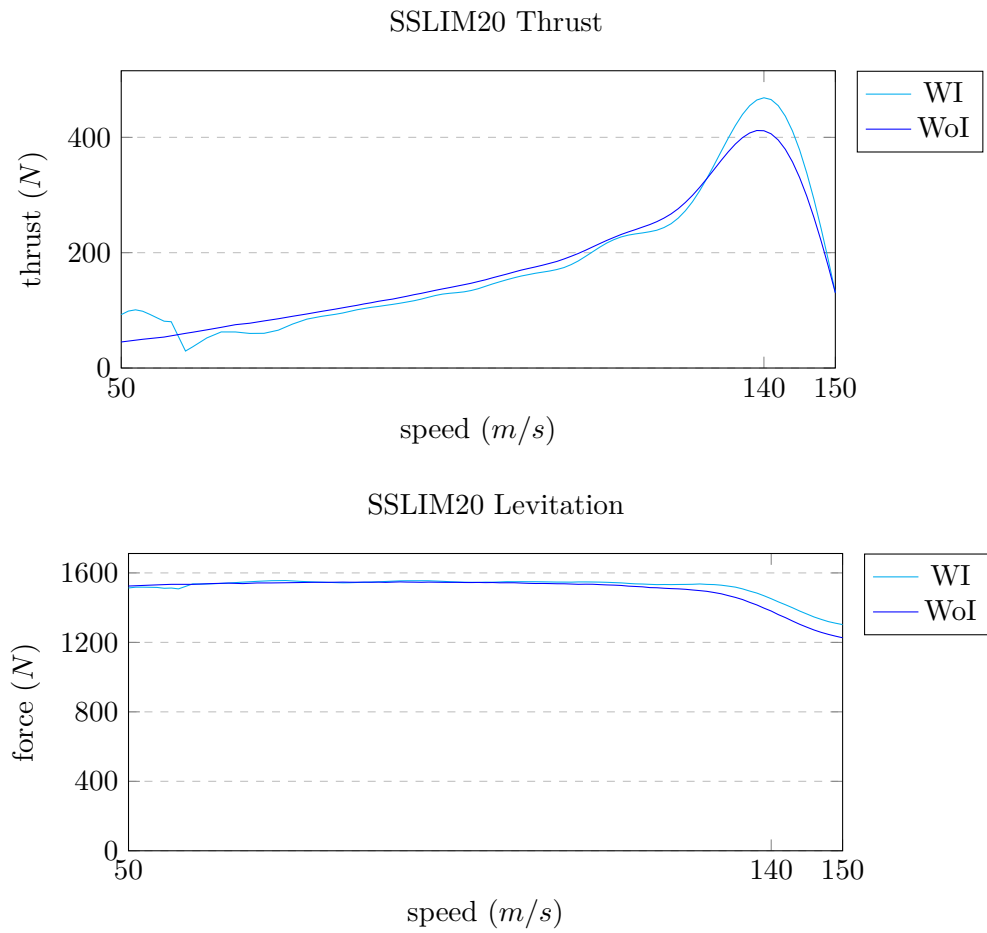

SSLIM20 Levitation

Figure 5.2: Thrust and repelling force with and without an iron backplate over speed at 800 Hz.

To investigate how good the stabilizing effects of such a levitating LIM are, a simulation with a variable air gap was set up. The repelling forces for air gaps of 1 mm to 7 mm are shown in Fig. 5.3. The design without an iron backplate was used for the simulation. The stabilizing effect can be seen as the force decreases with an increasing air gap.
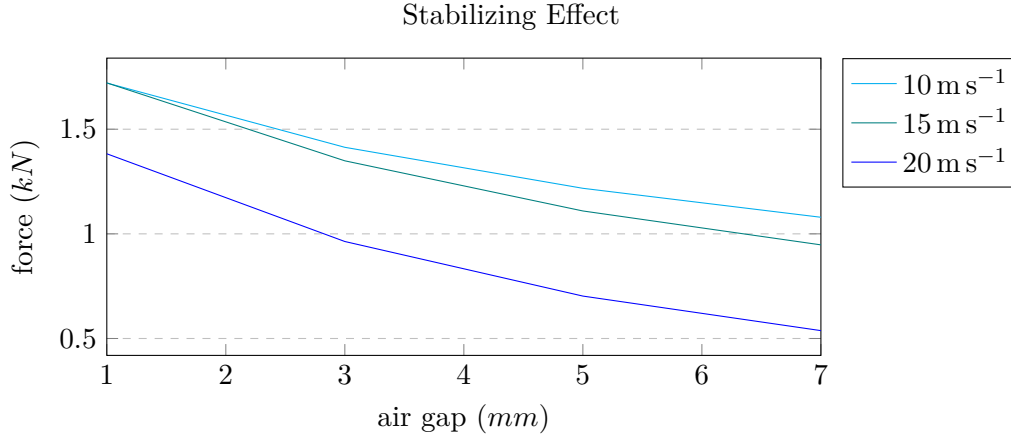

Figure 5.3: Repelling forces when varying the air gap.

5.2 Conclusion

The pod Swissloop designed is estimated to have a weight of 200 kg and a repelling force of at least 2 kN is needed to levitate successfully. Therefore, neither design is able to lift the pod. It's weight would have to get below 120 kg to achieve levitation. Alternatively, a longer LIM could be designed to have higher forces. However, this prolongs the pod and manufacturing might get more complicated.

If a lighter pod can be built, the repelling forces of the 6 pole-pair LIM might be sufficient to levitate. Varying the air gap showed promising results on the stabilizing effect of this type of levitation. However, the wheels can not be neglected totally as the repelling force decreases at low frequencies. So at the beginning of a run the pod must have wheels to support it. At higher speeds a lighter pod could levitate.

In the simulated designs the iron backplate improved both the thrust and repelling force. With increasing speed however the effect vanishes due to the skin effect in the secondary. Therefore, for high speeds the iron backplate is just additional weight that could be lost if the lower thrust at low speeds is acceptable.

6 Conclusion

In a first step the thrust theory of a LIM was investigated and implemented into a 1D analysis of a DSLIM. The results were then compared with 2D and 3D simulations using ANSYS Maxwell. The results showed the 1D analysis to be a powerful tool for multiple pole-pairs. However, to get accurate results end-effects must be included at higher speeds. For LIM with a low number of poles the end-effects are already significant at low speeds and the 1D analysis shows a big deviation from the simulations. When simulating in 2D the widening of the penetration width has to be taken into account to get accurate results and can be done using the Schwarz-Christoffel-Transformation. For the BabyLIM the simulations with Schwarz-Christoffel resulted in a maximum thrust of 400 N at 120 Hz. At lower frequencies a thrust of up to 800 N is expected. Testing of the LIM will show if these are accurate predictions.

For the LIM20 simulations of a pole-pitch-transition were done. With the proposed current switching a nice transition was achieved. Pole-pitch-transition is a great alternative to lowering the current if maximum voltage is hit. Higher thrusts can be achieved with it than by decreasing the current. If however the derivatives or the value of the current are different at the time of switching the frequency, voltage spikes occur and can cause damage to the system. Therefore, the control loops have to be carefully designed to switch at the defined instants.

In the last part of this thesis the repelling forces of the LIM20 were investigated and the possibility of levitating with this motor. 2D simulations showed increasing repelling forces with frequency. At 120 Hz a maximum of 1.3 kN is observed. This is not enough to lift the 200 kg pod. To be able to levitate either a bigger LIM has to be designed or the weight of the pod should not exceed 120 kg. In my opinion the possibility to use attraction forces by adding an iron sheet to the secondary should be investigated. Unfortunately this is not solely Swissloop's decision but it could be proposed to be included in the next test track.

6.1 Simulation Times and Mesh

Time is valuable and simulations can take up a lot of it. Therefore, a small summary of the duration of the simulations done in this thesis is given here. Simulation times are highly dependent on the machine they are done on. For this thesis some big simulations were done on the HPC cluster EULER. However, waiting times can be long on the cluster and therefore most of the simulations were done on a PC with the following system components.

Processor:	AMD Ryzen 7 3700X 8-Core/16-Thread
Mainboard:	Gigabyte X570
Memory:	32 GB DDR4-3200MHz
Grafics:	Radeon RX580

To account for system processes and to still have a responsive computer to work on while simulating only 12 threads were dedicated to ANSYS Maxwell. This allowed for 12 independent solution setups to run simultaneously. This means that for up to 12 simultaneously started setups, the time was not prolonged.

Most of the simulations were set up with a simulation step of 0.3 ms the simulated time however was adjusted accordingly to the need in every setup. Therefore, it is only interesting to compare the mean solution time for one step. This is given in Table 6.1. For completion the total time for one setup is listed as well.

	Type	time per setup	time per simstep
BabyLIM	2D	00:25:42	00:00:10
	3D	03:45:20	00:03:05
LIM20	2D	01:02:15	00:00:36
	3D	DNF	00:06:40
PPT	2D	02:00:00	00:01:20
Levitation	2D	02:10:00	00:01:50

Table 6.1: Mean simulation times for one solution setup.

Most simulations done in chapter 3 had 24 and more solution setups. Therefore, the simulations took at least two to three times the time per setup. A second thing that slowed the solution setup down was memory limits. The system had 32 GB Memory which was enough for all the 2D simulations. In 3D simulations this was exhausted quickly and the simulations slowed down or even aborted. Therefore, for 3D setups only two cores were permitted to allow for more memory per core and solution setup. This prolonged the computation for the 13 setups from two to seven times the time per setup. For the 3D simulation of the LIM20 the system aborted even with only one setup running. The error that was shown recorded that the solver has run out of memory and has therefore been killed. Unfortunately I could not look further into this topic as my time was limited.

The long simulation times especially in 3D led me to look into measures on how to speed up the simulations. Thereby I found out that mesh size and geometry have a big impact on the complexity of a simulation and therefore on the simulation time. As stated above, 6 mm was chosen as a maximum length for the solids. The vacuum was left to be meshed by the adaptive meshing of ANSYS, which is quite accurate. From simulations of previous years it was clear that an increase in the maximum mesh size would get less accurate results. At the beginning of this thesis I was not aware of the fact that, the current in a 2D design is only allowed to flow perpendicular to the plane. Therefore, the small gaps between the iron and the coils are not needed as insulation. This results in a simpler structure and a better mesh (Fig. 6.1). A similar simplification can be done in 3D with the boundary "insulation". It prevents a current flow perpendicular to the face it is applied to. As in 3D the current is allowed to flow in every direction, an "insulation" boundary can be applied to the faces where the current is not allowed to penetrate. This simplified the geometry and mesh similar to the 2D design by getting rid of the gaps between a coil and the core or other coils.

Further ideas to improve the geometry and mesh came up. It could be investigated on how a "skin depth layered based" mesh in the secondary I-beam would improve meshing and if it

affects the simulation results. Also, a different meshing in the teeth compared to the rest of the core might improve simulation time. Unfortunately there was not enough time to implement this into this thesis.

Other measures to speed up a simulation would be to use not only one core per setup but more if there are available cores. One test with a distribution of the solver process onto more than one core however led to impossible solutions and due to time constraints I did not further investigate this possibility.
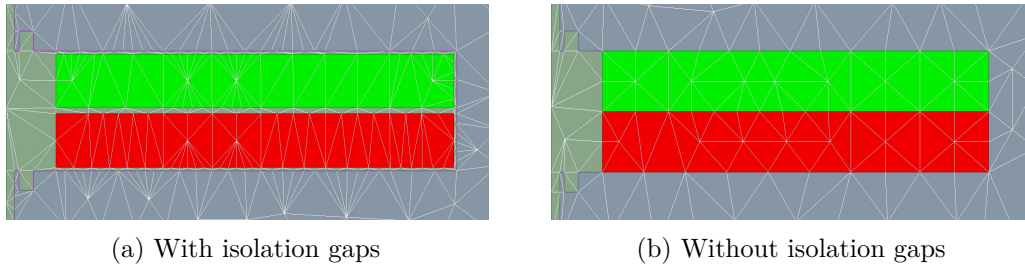

(a) With isolation gaps   (b) Without isolation gaps

Figure 6.1: Mesh in one slot in the 2D design.

6.2 Unfortunate Circumstances

Unfortunately, the lock-down due to COVID-19 caused delays in the assembly of the Baby-Pod. Working at ETH or EMPA was not possible until May 11th. Since then up until June 8th only limited work has been possible on the pod assembly due to social distancing. Under these conditions it was not possible to test the BabyLIM and compare the results with the simulations done. However, it opened the opportunity to look deeper into the simulations and extend it with simulations on the possibility to levitate with the LIM20.

6.3 Future Work

Other than integrating and testing the BabyLIM in the Pod, the effect of a pole-pitch-transition on levitation could be investigated. Unfortunately, pole-pitch-transition can not be tested accurately with the BabyLIM due to it having only one pole-pair. However, it would be interesting to see how the BabyLIM behaves when starting with 2 pole-pairs and then switch down to one. But first, this would have to be implemented in the control structure of the BabyPod.

Implementing end-effects into the 1D analysis would highly improve the accuracy of it and make it a valuable tool in designing the next LIM. Combining this analysis with the inverter and battery simulations could provide a powerful tool to optimize the entire system.

When further investigating levitation, an idea on how to improve thrust and levitation could be to introduce an iron layer on top of the I-beam and see if this results in the desired lifting force while still using a DSLIM to maintain thrust for high acceleration.

In terms of simulations a frequency domain simulation for LIMs might be interesting, as well as further investigations on how to reduce simulation times.

References

[1] eurostat, "Energy statistics," 2017. [Online]. Available: https://ec.europa.eu/eurostat/cache/infographs/energy/bloc-4a.html

[2] R. A. Buchmanan, "The atmospheric railway of i.k. brunel." *Social Studies of Science*, vol. 22, no. 2, pp. 231–243, 1992.

[3] E. Musk, "Hyperloop alpha," 2013. [Online]. Available: https://www.spacex.com/sites/spacex/files/hyperloop_alpha.pdf

[4] "Spacex hyperloop competition." [Online]. Available: https://www.spacex.com/hyperloop

[5] S. Yamamura, H. Ito, and Y. Ishulawa, "Theories of the linear, induction motor and compensated linear induction motor," *IEEE Transactions on Power Apparatus and Systems*, vol. PAS-91, no. 4, pp. 1700–1710, 1972.

[6] U. Bikle, L. Küng, and A. Colotti, "Electrical machines in mechatronics," ETH Zürich, Lecture Notes, 2019.

[7] "Swissloop." [Online]. Available: https://swissloop.ch

[8] M. Rogenmosser, "Inverter design for hyperloop linear induction motor," Laboratory for High Power Electronic Systems at ETH Zürich, Semester Thesis, 4 2020.

[9] J. Smajic, "Theory of linear induction motor (lim)," University of Applied Sciences Rapperswil, Lecture Notes, 2018/2019.

[10] T. D. Cox, "Development of novel linear drive machines," Ph.D. dissertation, University of Bath, 8 2008.

[11] "Electromagentics suite," ANSYS, 2019, version 2019 R3.

[12] A. Omlin, "Elektrische antriebssyteme i (german) [electrical drive systems i]," ETH Zürich, Lecture Notes, 2019.

[13] F. Krismer, "Design of power electronic systems," Power Electronic Systems Laboratory at ETH Zürich, Lecture Notes, 9 2019.

[14] P. Wiese, S. Luginbühl, L. Rufer, M. Krinner, A. Huwyler, T. Umbach, S. Eberhart, and F. Leuenberger, "Mid-term report swissloop," Institute for Dynamic Systems and Control ETH Zurich, Focus Project, 2 2020.

References

A Appendix

A.1 Python Program for 1D Analysis

```python
"""
1D Analysis of Linear Induction Motor

By Matthias Straessle
For a Semester Theses at ETHZ in 2020

"""
import cmath
import os
from math import pi

import matplotlib.pyplot as plt
import numpy as np
import scipy as sp
import scipy.signal as signal

#         |--------------------------------|
#         |    _      _      _      _      _     |
#         | R | |-T | | S | |-R | | T | |-S |
#         |    | |    | |    | |    | |    | |    |
#         |---| |---| |---| |---| |---| |---|
#-------------------------------------------------------------> x
#         |---------------->|
#                 T_p


#Variables [SI]
p = 6                    #polepairs
Toothwidth = 0.02    #20mm
Slotwidth = 0.0113    #12mm

T_p =3 * (Toothwidth + Slotwidth)
print(T_p)

n = 5000
t = np.linspace(0,1,n)
x = np.linspace(0, p * 2 * T_p,n)
# print(x[1])

mu_0 = 4*pi *1e-7
d_r = 0.0104
gap = d_r + 0.01
sigma_al = 2.5e7
I_peak = 150
N = 56
n_s = 2
```

```
47
48 k_w = 1 * np.sin(pi/3) #winding factor
49 a1 = 1.32
50
51 model_depth = 0.0532 #75mm
52
53 fig = plt.figure()
54 # magnetic flux in the windings (MMF) with spacial factor
55
56 for f_1 in np.linspace(40,120,3):
57     i = 0
58     w_1 = 2*pi*f_1
59
60     A = a1 * k_w * N*I_peak       # peak flux
61
62     O_tot = 3/2*A*np.exp(1j*(-w_1*t + pi/T_p*x))
63
64     v_s = 2 * T_p * f_1 #synchronous speed
65     print(v_s)
66     v = 0
67
68     F_x = []
69     F_plot = []
70     V_range = np.linspace(0,v_s-0.0001,400)
71
72     for v in V_range:
73
74         #Magentic field
75         B1 = (n_s * 3/2 *A)/(np.sqrt(((pi * gap/mu_0)*(pi * gap/mu_0))+(v_s - v
    )*(v_s - v)*(sigma_al * d_r*T_p)*(sigma_al * d_r*T_p)))
76
77         phi = np.arctan((pi * gap)/(mu_0 * sigma_al*d_r*T_p*(v-v_s)))
78
79         B_y = B1 * np.exp(1j*(-w_1*t + pi/T_p*x + phi))
80         #print(B_y.real)
81
82         # eddie currents
83
84         J_z = sigma_al*(v-v_s)*B_y
85         #print(J_z)
86
87         #Force
88         By = B_y.conjugate()
89
90         F_x.append((-model_depth* d_r * sigma_al * (v-v_s)* B1 * B1)*2*T_p* p)
91         # F_x.append(-model_depth* d_r * np.sum((J_z*By).real) * x[1])
92
93     #normalized all parameters
94     #fprint(max(F_x))
95     # F_x /= max(F_x)
96     # V_range /= 3.6 * v_s
97
98     F_plot.append(F_x)
99
100     plt.plot(V_range,F_plot[i],color ='blue', label = "$f_p$ = " + str(int(f_1)
    ) + " Hz")
101
```

```
102     # for j in range(len(V_range)):
103     #     if i%4 == 0:
104     #         print("(" + str(round(V_range[j],3)) + "," + str(round(F_plot[i][
        j],3))+ ")", end=' ')
105
106     # print('\n')
107
108     i+=1
109
110
111
112 legend = plt.legend()
113
114 plt.show()
```